AALBORG UNIVERSITY
DENMARK

Numerical Investigation of Pressure Retarded Osmosis with Brines for Power Generation

Kasper Juel Petersen
Fourth semester, Thermal Energy and Process Engineering, M.Sc.
Department of Energy Technology
Aalborg University

Thesis

Submitted in accordance with the requirements of the study regulations for a Master's thesis, at Aalborg University

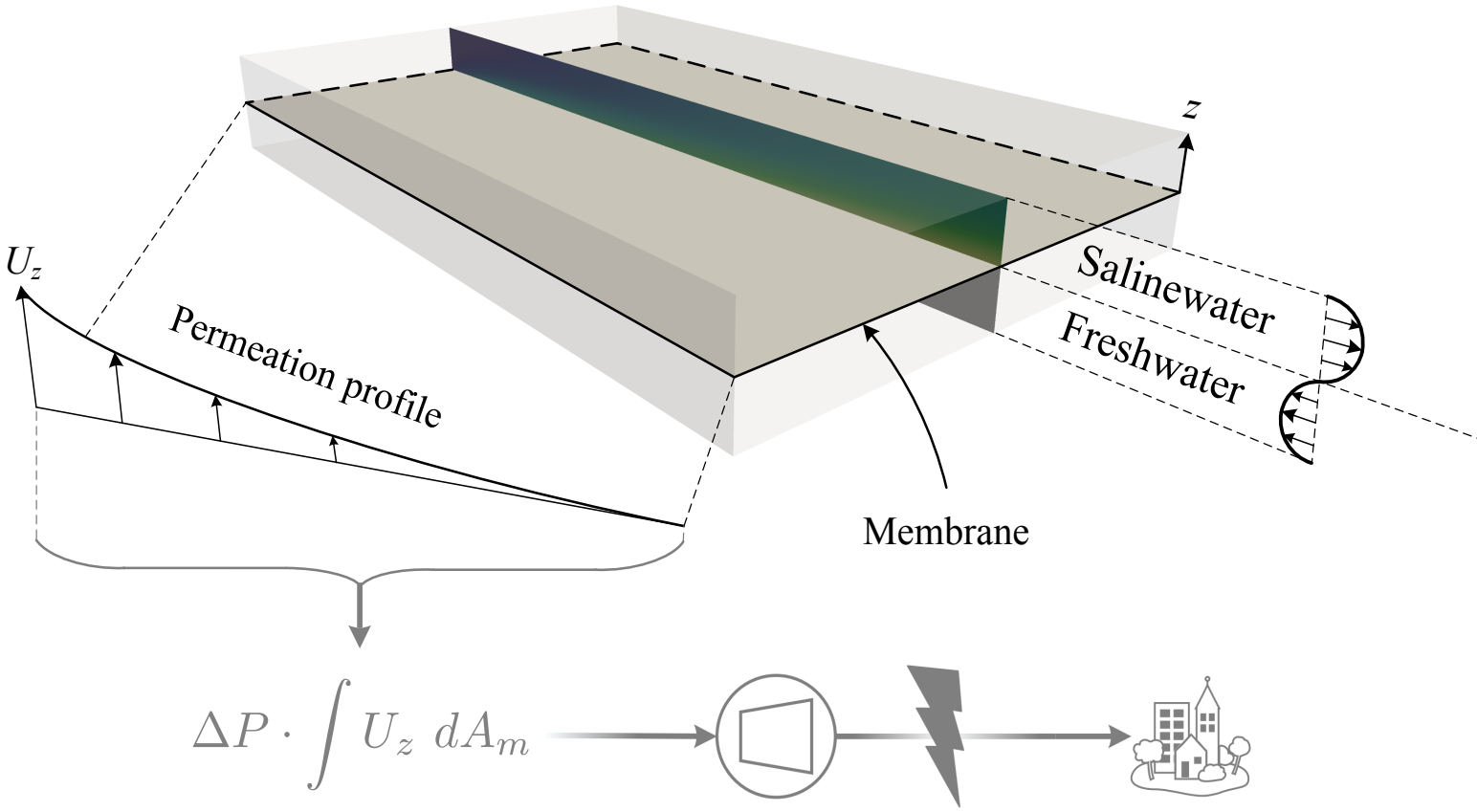

AALBORG UNIVERSITY
STUDENT REPORT

School of engineering and science
Energy Engineering
Pontoppidanstræde 111
9000 Aalborg
http://www.ses.aau.dk/

Title:

Numerical Investigation of Pressure Retarded Osmosis with Brines for Power Generation

Project:

Master's Thesis

Project period:

February 2018 - June 2018

Project group number:

TEPE4-1001

Author:

Kasper Juel Petersen

Supervisor:

Dr. Torsten Berning

Pages:

83

Appendices:

4

Project deadline:

June 1st, 2018.

Abstract:

In 2016 the global electric power consumption was 15567 TWh. A recent estimate claims that saline reservoirs contain salinity gradient power equivalent to 647 GW which amounts to 5668 TWh or 36.4% of the global consumption. For exploiting this energy reserve pressure retarded osmosis (PRO) has shown promise. PRO is a technology which can partially extract the energy from salinity gradients by separating a saline fluid from a pure/low-salinity fluid with a semi-permeable membrane. By implementing this membrane the trans-membrane gradients are converted into flow energy that can be extracted as mechanical work. The research presented in this report focuses on geothermal brines and shows that trans-membrane temperature differences between the geothermal and the low-salininty water similarly can be converted into mechanical work. Subsequently a phenomenological membrane model that can predict permeation rates based on the gradients is formulated and coupled with a computational fluid dynamics framework. The model can predict the effects of the important degradative phenomena of internal and external concentration polarization in terms of an energy flux loss. Performed simulations show that even a low solute mass fraction in the low-salinity stream of 1.39% yields an energy loss of 47%. Furthermore, it is concluded that trans-membrane gradients in temperature are not negligible and that the permeation rate exhibits a non-linear dependence on these. The model is the first to represent the effects of temperature gradients and the research has formed a basis for procuring a comprehensive framework which can predict membrane performance considering all fundamental driving forces. This will prove valuable for advancing the commercial implementation of the technology.

Preface

This thesis is written during the fourth semester on the Thermal Energy and Process Engineering M.Sc. programme from Aalborg University (AAU) in Denmark. The research is undertaken at the University of British Columbia Okanagan (UBCO), in Canada, in collaboration with *Dr. Joshua Brinkerhoff*'s UBCO Computational Fluid Dynamics Laboratory (http://okcfd.sites.olt.ubc.ca/).

Acknowledgements
I wish to express my gratitude towards my colleagues at UBCO, *Saeed Rahbarimanesh*, *Mohammad Haji* and *Shahab Zeraati*, whom I have had a pleasure of getting to know during my research in the UBCO CFD Laboratory, for their valuable advise and friendship.

I thank *Dr. Joshua Brinkerhoff* for his mentorship during my research and for being inspiring through his passion for science and technology, for supporting my aspirations and for inviting me to be a part of his research group in 2017/2018.

Similarly, to my supervisor, *Dr. Torsten Berning* from AAU, thank you for supporting me in pursuing my own research interest in this unconventional field and for your advice that has kept me on a continuously steep learning curve.

I am looking forward to crossing paths with you all in the future.

Author's signature

Aalborg University, June 1st, 2018

Kasper Juel Petersen
Email: kjpe13@student.aau.dk

Reading guide
The contents of the individual chapters in the report are introduced with a section written in *italic* font. Throughout the report all references are listed by the end of the report, in the bibliography. The references are denounced cf. the Harvard method, hence a statement will be referred by [surname(s), year]. If more than one reference from the same year has the same author, these are denoted with a, b, c etc. This reference refers to the bibliography where books are referred by author, title, ISBN-number, publisher, edition and year while websites are referred by author, title, year, URL and time of last visit. Technical papers are referred by author, title, year, journal name, volume, DOI. Figures, tables and equations are numbered according to the particular chapter they are placed in. The first figure in chapter three is consequently assigned with figure number 3.1 and the second 3.2 etc. Descriptive captions for tables are found above relevant tables and captions for figures are found under relevant figures. All units are given in terms of the SI metric system.

Contents

Nomenclature

The following nomenclature lists variable denotations used in the report, outlined in alphabetic order. The list comprises lower- and upper case Arabic notation, Greek notation and used abbreviations.

Symbol	Description	SI-unit
$\mathcal{A}$	Permeability coefficient	$m^3 \cdot m^{-2} \cdot s^{-1} \cdot Pa^{-1}$
$\mathcal{B}$	Salt permeability coefficient	$m^3 \cdot m^{-2} \cdot s^{-1}$
c	Specific heat	$J \cdot kg^{-1} \cdot K^{-1}$
C	Molar concentration	$mol \cdot m^{-3}$
D_h	Hydraulic diameter	m
e	Exponential	–
$\mathcal{D}$	Diffusion coefficient	$m^2 \cdot s^{-1}$
g	Gravitational acceleration	$m \cdot s^{-2}$
G	Gibbs free energy of mixing	J
h	Heat transfer coefficient	$J \cdot m^{-2} \cdot K^{-1}$
j_w	Permeation flux	$m^3 \cdot s^{-1} \cdot m^{-2}$
$k/\mathcal{K}$	Mass transfer coefficient	$m \cdot s^{-1}$
K	Sorption coefficient	–
$\mathbf{K}$	Permeability tensor	–
L	Length	m
MW	Molar weight	$kg \cdot mol^{-1}$
M	Chemical potential	$J \cdot mol^{-1}$
n	Molar amount	mol
$\mathbf{n}$	Wall normal vector	–
P	Pressure	Pa
PD	Power density	$W \cdot m^{-2}$
Q	Heat flow	$J \cdot s^{-1}$
R	Universal gas constant	$J \cdot mol^{-1} \cdot K^{-1}$
$\mathcal{R}$	Solute resistivity	$s \cdot m^{-1}$
Re	Reynolds number	–
$\mathcal{S}$	Structure parameter	m
s	Molar specific entropy	$J \cdot mol^{-1} \cdot K^{-1}$
$S_w^{\int_t dT}$	Molar absolute entropy	$J \cdot mol^{-1}$
S	Saturation	–
S	Source term	–
T	Temperature	K
t	Thickness	m
U	Velocity	$m \cdot s^{-1}$
v	Molar specific volume	$m^3 \cdot mol^{-1}$
x	Direction along membrane length	m
y	Direction along membrane width	m
z	Direction along membrane height	m

ρ	Density	$kg \cdot m^{-3}$
π	Absolute osmotic pressure	Pa
α	Thermal diffusivity	$m^2 \cdot s^{-1}$
β	Van't Hoff factor	–
ζ	Slip coefficient	–
η	Efficiency	–
γ	Activity coefficient	–
ω	Mass fraction	–
χ	Mole fraction	–
τ	Tortuosity	–
κ	Permeability	–
∇	Gradient	s^{-1}, m^{-1}
ε	Porosity	–
μ	Dynamic viscosity	$N \cdot s \cdot m^{-2}$
ν	Kinematic viscosity	$m^2 \cdot s^{-1}$

Abbreviation	**Description**
BC	Boundary condition
CDS	Central difference scheme
CFD	Computational fluid dynamics
CP	Concentration polarization
CTA	Cellulose triacetate
CV	Control volume
C-ECP	Concentrative external concentration polarization
D	Draw side
DSC	Draw solution concentration
D-ECP	Dilutive external concentration polarization
ECP	External concentration polarization
F	Feed side
FO	Forward osmosis
FS	Flat sheet
FVM	Finite volume method
GAMG	Geometric-algebraic multi-grid
HF	Hollow fibre
ICP	Internal concentration polarization
ID	Inner diameter
OD	Outer diameter
OF	OpenFOAM
PD	Power density
PRO	Pressure retarded osmosis
PX	Pressure exchanger
RO	Reverse osmosis
SIMPLE	Semi-implicit method for pressure-linked equation

Introduction

1

This chapter aims to describe the motivation for the performed research, identify problems and possible solutions in furthering the pressure retarded osmosis (PRO) technology and to present the state of the art and the scope of this project.

The motivation for studying PRO within the framework of this study is multifold, considering the many advantageous properties of the technology. Firstly, the global demand for energy is on a steady rise as a consequence of economic development and a rapid growth in human population. With an inevitable depletion of the worlds shale oil reservoirs a pronounced incentive for research in novel renewable energy technologies which are independent of fossil fuels should be predominant in academic communities and in industrial and political organizations. Yet still, due to the low cost of refined fossil fuels the general population seem to be lacking in their commitment to the responsibility of leaving a minimal/no footprint on the environment for future generations.

For this reason it is extremely important that more attention is brought to the potential of renewable energy sources in order to mitigate the emissions of green house gasses. In 2016 the worldwide consumption of electric energy alone was reportedly equivalent to 15567 TWh [IEA, 2017]. A recent estimation on the potential of salinity gradient power, which is the theoretical limit for what is extractable, is brought forward by Alvarez-Silva et al. [2016]. The estimate is 647 GW in continuous power equivalent to 5668 TWh p.a. or 36.4% of the worldwide consumption of electricity, as of the 2016 figures. This constitutes the first incitement to do research in this particular technology.

Moreover, the technology poses a relatively small environmental impact if the technology is implemented in a location with abundant water resources. The disposal of the working fluid for the system can be problematic considering the constituents of geothermal fluids. Especially if the brine is extracted from abandoned shale wells, after fracking. However, novel technology for diluting the discharge from prospective PRO plants is in development.

1.1 Salinity gradient energy and osmotic power

1.1.1 Idealized osmotic processes and exergy in saline fluids

The energy in saline gradients is attributed to the difference in the salt concentrations of two fluids of different chemical compositions and thereby the individual chemical potentials of either fluid. When the two fluids mix naturally the chemical potential is lost irreversibly and no work is produced from the process. A semi-permeable membrane can be used to partially extract the chemical potential. This is the key concept in PRO. The chemical potential is a molecular

contribution to the energy of mixing, for which the maximum available energy is the Gibbs free energy of mixing, $\tilde{\Delta}G$. This energy is defined by equation (1.1).

$$\tilde{\Delta}G = \tilde{\Delta}H - T \cdot \tilde{\Delta}S \tag{1.1}$$

Here, $\tilde{\Delta}H$ is the enthalpy of mixing, T is the absolute temperature and $\tilde{\Delta}S$ is the contribution in entropy of mixing to the total entropy of the corresponding solution of the constituents in the mixing process. The total entropy change can be written as per equation (1.2) in which R is the gas constant and χ_i is the mole fraction of the i'th species in the solution.

$$\tilde{\Delta}s = -R \sum_i \chi_i \ \ln \chi_i \tag{1.2}$$

Denoting the saline with subscript D for the draw stream and the low concentration solution F for feed stream, and assuming that the solution of the two, denoted M, is binary, and that the enthalpy of mixing is constant, the maximum theoretical attainable energy of mixing is as in equation (1.3).

$$\begin{aligned} \tilde{\Delta}G &= \cancelto{0}{\tilde{\Delta}H} + \Delta G_M - (\Delta G_D - \Delta G_F) \\ &= -(n_D + n_F) \cdot T\tilde{\Delta}s_M + \left(n_D \cdot T\tilde{\Delta}s_D + n_F \cdot T\tilde{\Delta}s_F\right) \end{aligned} \tag{1.3}$$

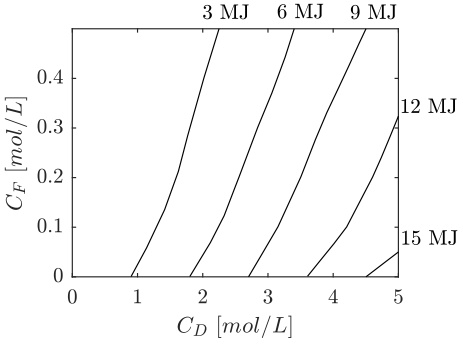

Figure 1.1: Iso-contours of Gibbs free energy for different feed and draw concentrations, C_F and C_D, at $T = 293$ K.

From this, researchers such as Kuleszo et al. [2010] have approximated the theoretical available energy from the mixing of 1 m^3 of fresh water with 1 m^3 of a NaCl-water solution. Their results are depicted in Figure 1.1. The magnitude of their results are confirmed by Alvarez-Silva et al. [2014] who estimate, that the chemical potential between a seawater reservoir and a fresh water stream with a flow rate of 1 $m^3 \cdot s^{-1}$ contains mixing power equivalent to 2.5-2.7 MW.

These numbers do however serve as theoretical limits and the extractable energy is dependent of the draw (in PRO: saline fluid) and feed (in PRO: fresh water) temperatures, the extent to which the two solutions are mixed and the amount of diabatic energy loss. Nevertheless, the figure shows how large the potential of saline gradient energy is, if technology for its extraction is developed further.

The chemical potential is proportional to the amount of energy that can be absorbed or released during a reaction between two or more species, or during phase change. An osmotic pressure differential $\Delta\pi$ arises as a consequence of the chemical potential between two species, and it is what drives the diffusion of either species. Eventually the two species mix completely into one uniform solution in chemical equilibrium.

It is this osmotic pressure that constitutes a major fraction of the driving force in the PRO technology, and the permeation is strongly dependent on this and the static pressures of the draw and feed streams. PRO is one of three processes driven by the osmotic pressure and defined by the magnitude of the applied pressure difference between the draw and feed streams. The other two

processes are forward osmosis (FO) and reverse osmosis (RO). All of these utilize semi-permeable membranes, i.e. membranes that are permeable to the solvents but impermeable to the solutes. Figure 1.2 illustrates the three osmotic processes. In the schematic the semi-permeable membrane is in the center separating two reservoirs. One side has a lower concentration of solutes compared to the other side. The membrane is assumed to consist of an active layer (black, the selective layer, that is actually semi-permeable) and a support layer (white, permeable to both solvent and solutes with higher porosity). FO is the naturally occurring process, where $\Delta P = P_D - P_F = 0$. Here $\Delta\pi$ is the primary driving force that constitutes the permeation rate.

If a pressure is applied to the saline side, the permeation rate is augmented following a polynomial progression until it saturates at an arbitrary maximum limit, at an intermediate pressure close to $\Delta P \sim {}^1\!/_2\Delta\pi$. Increasing the pressure further after the maximum, decreases the permeate flux until $\Delta P \to \Delta\pi$. The osmotic process is termed as pressure retarded in this interval, i.e. $\in\ ]\Delta P = 0, \Delta P = \Delta\pi[$. Increasing the differential pressure above the osmotic pressure causes reversal of the permeation direction, inducing energy intensive reverse osmosis. Where $\Delta\pi = \Delta P$, the system is in osmotic equilibrium with the trans-membrane permeation flux being zero [Wijmans and Baker, 1995].

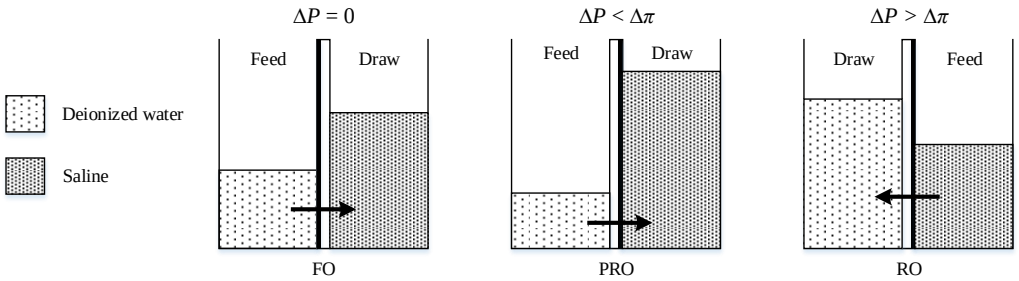

Figure 1.2: Illustration of the three osmotic processes forward osmosis, pressure retarded osmosis and reverse osmosis. The bold line in the membrane represents the active layer. The remaining membrane material is assumed to be a non-selective porous support layer. When the flow direction reverses going from PRO to RO, the original draw stream becomes the feed, and vice versa, by the convention used by Wijmans and Baker [1995]. Aschmoneit [2016] states that the active and support layers of a typical FO membrane have thicknesses of $t \sim 150$ nm and $t \sim 150$ μm, respectively.

For PRO, the trans-membrane permeation flux is conventionally formulated as in equation (1.4). This relation is the simplest permeation equation for which the utilized membrane is perfectly selective and the solute concentration close to the membrane is equal to the bulk concentration. The latter is unrealistic due to inhibitive phenomena such as external concentration polarization (ECP) which constitutes one of the irreversibilities introduced to the process. This is described in detail below. In the equation j_w is the idealized permeation flux, $\bar{\pi}_D$ is the bulk osmotic pressure of the draw solution, $\bar{\pi}_F$ is the bulk osmotic pressure of the feed solution, ΔP is the pressure differential across the membrane and $\mathcal{A}$ is the solvent permeability coefficient which represent the actual physics that govern the transfer of static pressure into permeate momentum.

$$j_w = \mathcal{A} \cdot (\bar{\pi}_D - \bar{\pi}_F - \Delta P) = \mathcal{A} \cdot (\Delta\pi - \Delta P) \tag{1.4}$$

1.1.2 Irreversible osmotic processes and inhibitive phenomena

The reason as to why the Gibb's free energy is only partially extractable is due to the following inhibitive phenomena [Touati et al., 2017] that are depicted in figure 1.3:

1. Internal concentration polarization (ICP).
2. External concentration polarization (ECP).
3. Reverse salt flux, j_s.

In PRO membranes, porous support layers are used to make the active layer withstand high pressures $\mathcal{O}\left(10^2 \text{ bar}\right)$ within a membrane module. The cross-sectional area of the pores in the support layer make both the solvents and solutes permeable to those layers. However, when the solutes are incident at the internal wall of the active layer, they are blocked by the selectivity of the layer and thus accumulate at the surface. This is referred to as ICP which is proportional to an unextractable fraction of the chemical potential. The equivalent increase to the internal concentration C_i is depicted in figure 1.3.

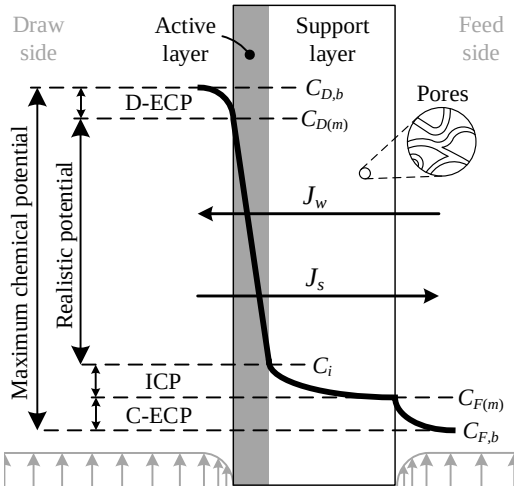

Figure 1.3: Chemical potentials and their losses to concentration polarization, and permeate and salt fluxes.

At the surface of the active layer, on the draw side of the membrane, the boundary layer is displaced in the wall normal direction because of the permeation of fresh water. It is the local concentration, incident at the active layer that governs the permeation, not the bulk concentration. This also amount to a loss in chemical potential and is termed dilutive ECP (D-ECP).

Even though the support layer is permeable to solutes, they still accumulate at the interface between the feed stream and the support layer which increases the local concentration resulting in concentrative ECP (C-ECP). The effect is pronounced with higher solute concentrations in the feed stream. Moreover, due to the large osmotic pressure gradient, a small amount of salt does permeate through the active layer, in the opposite direction of the permeation. This characterizes a real and imperfect active layer.

In summary, an infinitely long and ideal membrane with no ICP, ECP or reverse salt flux can extract the theoretical Gibb's free energy, but membrane technology is not sufficiently developed to provide a platform for this. In reality, the permeation is defined from the concentrations around the active layer, $C_{D_{(m)}}$ and C_i, so that the realistic permeation rate is j_w in equation (1.5), defined by a mitigated osmotic pressure difference $\Delta\pi = \pi_{D_{(m)}} - \pi_i$. The reverse salt flux is as in equation (1.6).

$$j_w = \mathcal{A} \cdot \left(\pi_{D_{(m)}} - \pi_i - \Delta P\right) \tag{1.5}$$

$$j_s = \mathcal{B} \cdot \left(C_{D_{(m)}} - C_i\right) \tag{1.6}$$

$\mathcal{B}$ is the salt permeability which represents the physics that describe the reversed flow of salt. The reverse salt flux and the permeate flow rate are related through relation (1.7) [Touati et al., 2017]. Here is β the Van't hoff coefficient for the solute in a binary mixture [Çengel and Boles, 2011].

$$j_s = \frac{\mathcal{B}}{\beta \cdot R \cdot T}\left(\frac{j_w}{\mathcal{A}} + \Delta P\right) \quad \leftrightarrow \quad \frac{j_s}{j_w} = \frac{\mathcal{B}}{\mathcal{A} \cdot \beta \cdot R \cdot T}\left(1 + \frac{\mathcal{A}\Delta P}{j_w}\right) \tag{1.7}$$

1.2 Utility scale extraction of osmotic power

To depict a basic implementation of the membrane technology, a conventional plant setup is presented in the following. A plant layout for PRO is depicted in figure 1.4. The plant is simplified and a large-scale operation will require several units of circulation pumps, pressure exchangers (PX) and membrane modules. Starting with the draw solution, which in this project is geothermal water with a significantly higher salinity compared to sea water, the draw stream is first pre-treated with e.g. sand filters and bag filters to avoid larger solid particles from entering the membranes. After obtaining a pressure increase in the low pressure side of the PX, the draw stream enters a membrane module where it is mixed with the permeate, from the feed stream, creating a large increase in volumetric flow rate. After this, the stream is split with a fraction of the flow being led back to the high pressure side of the pressure exchanger, where the hydraulic energy generated from circulation pumps is recovered and fed back into the draw stream. This pressure recovery technology is adopted from RO plants and account for large savings in pumping power, considering that the hydraulic pressure in the draw stream approaches 100 bar. The kinetic energy in the remaining draw solution is extracted in a hydro turbine. The discharge at the draw side of the membrane is still brackish, i.e. it has an intermediate salinity, due to the process being irreversible.

It is very important that the feed solution is pretreated for solid particles, as the support layer is directly exposed to the feed stream and it is herefore extremely susceptible to ICP. At the outlet of the membrane module the feed side is bled by a fraction of the initial feed rate.

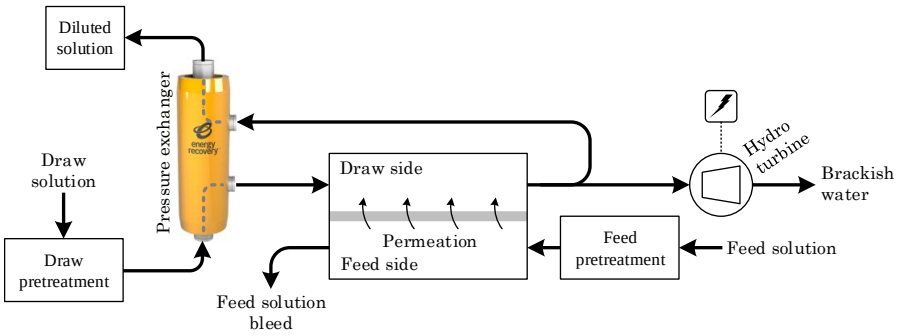

Figure 1.4: Schematic of a conventional PRO plant.

It is at this point noted, that this investigation will not go deeper into the aspect of plant processes of the technology, but rather the membrane flow physics. This section should however give a basic outline of the principles constituting the facility for the energy conversion.

1.3 Modelling of the permeation in osmotic processes: A state of the art review

Prior to choosing the modeling methodology for this study, an overview of various approaches to permeation modelling is brought forward. From this, underlying assumptions for necessary modeling simplifications, efficiently defined boundary conditions and appropriate solvers are identified and outlined. The focus for the available modeling frameworks will be computational fluid dynamics (CFD), as applying the finite volume method (FVM) from an early point on, is identified as an appropriate and yet comprehensive way of modeling the membrane process. For the last two decades, serious efforts have gone into the CFD modeling of FO and RO, as the two technologies have a projected potential in remediating the increasing demand for clean drinking water world wide. However, to the knowledge of the present author, very few advanced models of the flows in PRO processes have been developed to answer questions concerning concentration polarization, permeation rate dependence and the degrading effects of reverse salt flux. Specifically the authors who have aimed to model PRO with CFD are Hayashi and Okumura [2016]; Wang et al. [2016]; Li [2015], and they only tailor their models to represent lower osmotic pressure corresponding to brackish solutions.

Due to the mechanisms that constitute the driving force for permeation across a membrane being inherently complex, a fully coupled approach with phenomenological modeling for e.g. thermophysical properties is preferred. Considering the water permeability ($\mathcal{A}$) and reverse salt flux ($\mathcal{B}$) coefficients in equation (1.4), correlations for these coefficients that represent the governing physics behind the permeation rate, cf. equations (1.8) and (1.9), should be coupled with the governing Navier-Stokes equations. E.g. $\chi_{w,0}$ and v_w are both dependent on the solute transport and weak compressibility of the draw side solution.

$$\mathcal{A} = \frac{\mathcal{D}_w \cdot K_w \cdot \chi_{w,0} \cdot v_w}{t \cdot R \cdot T} \qquad (1.8) \qquad \mathcal{B} = \frac{\mathcal{D}_s K_s}{t} \qquad (1.9)$$

The derivation of the two coefficients is presented in appendix A on page 69. It is from here evident that the coefficient definitions are inferred from chemical potentials in the spatial gradients of hydraulic pressure and solute concentration. Ultimately, the derivation yields the relation for permeate flux, j_w, equation (A.1) (and equation (1.10)).

$$j_w = \mathcal{A} \cdot (\Delta\pi - \Delta P) \qquad (1.10)$$

The flow energy in the permeate per area membrane is defined as in equation (1.11) and referred to as the power density (PD).

$$PD = j_w \cdot \Delta P = \mathcal{A} \cdot \left(\Delta\pi\Delta P - \Delta P^2\right) \qquad (1.11)$$

From this relation the optimum operating hydraulic and osmotic pressures can be found. The relation is a polynomial function of the hydraulic pressure difference, i.e. the gradient of ΔP can be used to achieve the maximum achievable power density:

$$\mathcal{A} \cdot \left(\Delta\pi\Delta P - \Delta P^2\right) \cdot \frac{d}{d\Delta P} = 0 \quad \rightarrow \quad \mathcal{A} \cdot (\Delta\pi - 2 \cdot \Delta P) = 0 \qquad (1.12)$$

The solution to equation (1.12) and therefore then pressure at which the maximum power density is attainable, is $\Delta P = \frac{1}{2}\Delta\pi$. Mostly, the power density is approximated through experiments where

the nature of all inhibitive phenomena are manifested in the results. However, with numerical investigations these ought to be inferred through correlations for $\mathcal{A}$ and $\mathcal{B}$ as these are spatially varying throughout the membrane. They are in many works available in academic literature assumed to be constants, but the present author is confident that the importance of their implicit formulation into the framework of a prospective permeation model is important.

Moreover, by convention the temperature gradient is not inferred in the derivation of j_w (through the chemical potential, in equation (A.3)). This is justifiable considering that in e.g. a RO process, the feed stream (river water) and the draw stream (seawater) are at comparable temperatures. In the perspective of this study, the draw stream is assumed to be a brine from a geothermal well, meaning that the temperatures can be in excess of 40°C. This results in a rather strong temperature gradient when the feed stream in e.g. winter is as low as 2°C. Experimental analyses on the temperature gradients effect on the osmotic performance have been performed by researchers such as Phuntsho et al. [2012] and Traxler [1928], who all conclude that the temperature gradient is a strong driver for enhancing permeation flux. Thus, this optimially should be implemented into a prospective permeation model.

Assuming *a priori* that the power density will be a function of $\Delta\pi, \Delta P$ and ΔT, the trivial solution of $\Delta P = {}^1\!/_2\Delta\pi$ is no longer valid in the scope of this study as it is based on the assumption of a negligible temperature gradient. Li [2015] confirms that the temperature gradient does shift the optimal point of ΔP away from ${}^1\!/_2\Delta\pi$. To the present authors knowledge, no models including the temperature dependence exists. This makes said dependence an interesting aspect to mathematically and numerically examine.

1.3.1 Studies on thermal effects in salinity gradient technologies

In the following, a presentation of the effects of a temperature gradient is given, with the aim of quantifying the extend of osmotic enhancement from thermal effects. She et al. [2012] investigates the effects of higher bulk temperatures without a temperature gradient and they report an increase in the permeability coefficient at higher temperatures. This means that the enhancement from various temperatures is not only attributed to the difference in chemical potential between to streams.

Touati et al. [2015b] seek to isolate thermal effects from the temperature gradient, and their findings show that gradient potential is significant for the permeation flux. Their main results are depicted in figures 1.5 and 1.6. The framework they apply to determine the permeation coefficients is presented in section 1.3.5 on page 23. In figure 1.5 the hydraulic pressure difference is varied at three different temperature levels in one stream, whilst the other is kept isothermal, i.e. the left hand side figure shows the effect of varying the feed side temperature, and the right hand side figure the draw side temperature. It is noticeable that there is a relatively consistent permeation gain of $\delta\mathcal{A} \sim 0.5 \cdot 10^{-12}$ per 10 K feed stream temperature increase across the entire pressure range, and that at higher pressures, the permeability is almost doubled with a 20 K temperature increase. Varying the draw side temperature instead of the feed side temperature has a lesser impact on the permeability coefficient.

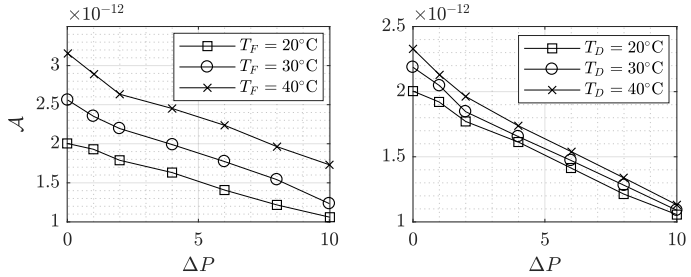

Figure 1.5: Effect of varying draw and feed side bulk temperatures, on the permeability coefficient. In the figure on the left hand side, $T_D = 20°C$, and similarly for the other, $T_F = 20°C$ [Touati et al., 2015b].

The pronounced difference in varying the temperatures of either side of the membrane can be explained from the topology and behaviour of the active layer and the porous support. The utilized membrane in the experiments of [Touati et al., 2015b] is of the same configuration depicted in figure 1.3 on page 14, with the active layer facing the draw stream, and the more pervious substrate facing the feed stream. The essential difference is that the heat transfer through the porous support is governed by both conduction and advection, whereas the active layer acts as a thermal barrier primarily allowing conduction. The advection is in the direction from the feed stream towards the draw, meaning that a significant amount of heat is transferred in this flow and is therefore easily transported into the support material. The material is elastic and deforms under thermal stress which dilates its pores. This changes the void volume in the material, and subsequently accommodates a higher permeation of solvent. As the pores dilate, solute particles experience a lower friction and are inhibited to a lesser extend, in their path from the draw stream to the feed stream. This explains the trends in figure 1.6 which depict higher reverse salt permeability with higher temperatures.

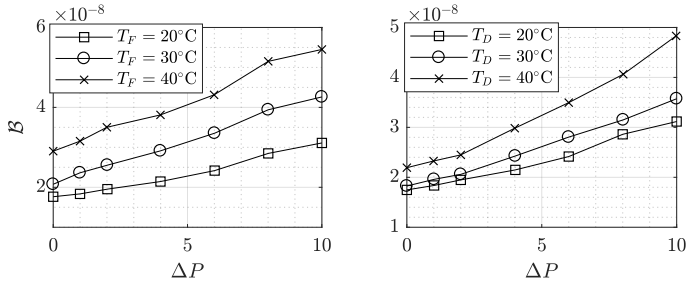

Figure 1.6: Effect of varying draw and feed side bulk temperatures, on the reverse salt flux coefficient. In the figure on the left hand side, $T_D = 20°C$, and similarly for the other, $T_F = 20°C$ [Touati et al., 2015b].

A preliminary assumption is brought forward: Permeation rate is significantly dependent on the sign of the temperature gradient and the membrane configuration. Considering the simultaneously increasing permeability coefficients, a multi-variable optimization problem occurs where the max performance is constituted by a maximized $\mathcal{A}$ where $\mathcal{B}$ is still limited enough to mitigate the degrading effects of ICP.

The results only depict the variation in the permeability coefficients at relatively low hydraulic pressures, and extrapolating the same $\frac{\delta \mathcal{A}}{\delta T}$ to higher pressures (~ 100 bar) might not be realistic as a higher hydraulic pressure account for an increasing fraction of the total driving force on the permeate.

1.3.2 Published works and software within the OpenFOAM framework that are adoptable for numerical modelling of PRO

Gruber et al. [2011] aim to qualitatively estimate the effects of ECP whilst assuming that $\mathcal{A}$ and $\mathcal{B}$ are constants, and $\pi, \mathcal{D}_{sw}, \nu$ and ρ are linearly dependent on the mass fraction, ω_s. In the authors' work, the effects are investigated in a FO setup through parametric studies with varying solute mass fractions, draw flow rates and slip velocities. The external concentration is quantified by the displacement of the solute mass fraction profiles, in the normal direction of the membrane surface. It is found, even without the effects being incorporated through $\mathcal{A}$, that concentration polarization is more predominant than other researchers often assume. Implemented in the authors' framework, are the governing equations for conservation of mass (1.13), momentum (1.14) and solute mass fraction (1.15). The latter is the one that represent the mixing between the solute and solvent phases and subsequently determines the extent of ECP.

$$\frac{\partial \rho}{\partial t} + \nabla \cdot (\rho \mathbf{U}) = 0 \tag{1.13}$$

$$\frac{\partial \rho \mathbf{U}}{\partial t} + \nabla \cdot (\rho \mathbf{U}\mathbf{U}) = \nabla \cdot \mu \cdot \left(\nabla \mathbf{U} + \nabla \mathbf{U}^T \right) - \nabla P + \rho \mathbf{g} \tag{1.14}$$

$$\frac{\partial \rho \omega_s}{\partial t} + \nabla \cdot (\rho \mathbf{U} \omega_s) = \nabla \cdot (\rho \mathcal{D}_{sw} \cdot \nabla \omega_s) \tag{1.15}$$

In these, ρ is the density, t is time, $\mathbf{U}$ is the velocity vector, μ is the dynamic viscosity, P is the absolute pressure, $\mathbf{g}$ is the gravitational acceleration vector, ω_s is the solute mass fraction and $\mathcal{D}_{sw}$ is the binary diffusion coefficient. These three equations are used to represent the transport in the draw and feed streams, whilst the permeation through the porous medium is modeled rather than resolved. This is done cf. the Loeb permeation model, equation (1.16) for FO membranes [Loeb et al., 1997].

$$j_w = \frac{1}{\mathcal{R}} \cdot \ln \left(\frac{\mathcal{B} + \mathcal{A} \cdot \pi_{D_{(m)}}}{\mathcal{B} + |j_w| + \mathcal{A} \cdot \pi_{F_{(m)}}} \right) \tag{1.16}$$

Here, $\mathcal{R}$ is the resistivity of the solute to diffusion in a porous substructure, $\mathcal{B}$ is the reverse salt flux coefficient, $\mathcal{A}$ is the permeation coefficient, π is the osmotic pressure and subscript (m) denotes the membrane medium. It is noticeable that the permeation flux in this model is only dependent on the osmotic pressure. This makes it invalid for PRO membrane permeation as this is dependent on the hydraulic pressures as well. However, the rest of the framework does still apply, due to the similarities between PRO and FO, i.e. identical permeate flux directions and geometric membrane designs (concentric tubular membranes). The differences between the modes, being salinities, forward facing direction of the active layer, and the hydraulic pressures can be modeled through a permeation model. To accomodate closure for the framework a set of linear equations

is adopted from Geraldes et al. [2001] to model the osmotic pressure (1.17), the dynamic viscosity (1.18), the binary diffusion coefficient (1.19) and the weak compressibility (1.20):

$$\pi = 805.1 \cdot 10^5 \cdot \omega_s \quad \propto \quad \beta RT \cdot \omega_s \tag{1.17}$$

$$\mu = 0.89 \cdot 10^{-3} \cdot (1 + 1.63 \cdot \omega_s) \tag{1.18}$$

$$\mathcal{D}_{sw} = \max\left(1.61 \cdot 10^{-9}\left(1 - 14 \cdot \omega_s\right), 1.45 \cdot 10^{-9}\right) \tag{1.19}$$

$$\rho = 997.1 + 694 \cdot \omega_s \tag{1.20}$$

These are only valid for $\omega_s \in [0, 9]\%$, i.e. the applicability of the relations to higher salinities can not be advocated for. Researchers Touati et al. [2015a] state that temperature and solute-concentration dependent thermophysical properties, such as viscosities, diffusivities etc., alter the permeation flux, i.e. they should not be assumed constant, and justified correlations should be used in a prospective model. The osmotic pressure is similarly a function of concentration and temperature:

$$\pi = \beta \cdot R \cdot T \cdot C = \varphi \cdot C \tag{1.21}$$

Moreover, a solute fraction balance is employed through equation (1.22) to ensure conservation throughout the computational domain:

$$-\rho_{(m)} \cdot \mathcal{D}_{sw} \cdot \frac{\partial \omega_s}{\partial n}\mathbf{n} + \rho_{(m)} \cdot \omega_{w_{(m)}} \cdot j_w = j_s \tag{1.22}$$

The reverse salt flux j_s, is solved according to equation (1.23), where $\varphi = \beta \cdot R \cdot \bar{T}$. The relation is inferred from relations (1.5) and (1.6), assuming a zero pressure gradient over the membrane.

$$j_s = \frac{\mathcal{B}}{\varphi \cdot \mathcal{A}} \cdot j_w \tag{1.23}$$

As the boundary layer over the membrane surface in the draw side is disrupted by the percolation of permeate, a traditional boundary layer development cannot be assumed, and neither can a no slip condition on the wall. To infer slip velocities $\mathbf{U}_{\text{slip}}$ within the boundary layer, equation (1.24) is implemented:

$$U_{\text{slip}} = -\frac{\sqrt{\kappa}}{\zeta} \cdot \frac{\partial \mathbf{U}}{\partial \mathbf{n}} \tag{1.24}$$

ζ is a slip coefficient which describes the hydrodynamics within and adjacent to the active layer from characteristic parameters such as material roughness, porosity and tortousity, and κ is the permeability. As the osmotic mode is implemented through the usage of a permeability model, such as (1.16), the framework formulated by Gruber et al., can be adapted for the PRO mode. The researcher Aschmoneit [2016] proposes an implementation with hydraulic pressure dependence for bent membranes, based on the software developed by Gruber et al. (whereas their code only works for flat sheet membranes).

The reason why permeation models are applied is due to the computationally prohibitive demands of resolving the Stokes flow on a nano scale, within a porous medium and the formulation of

appropriate boundary conditions. Coupling this with the flows in the draw and feed streams is prohibitive considering the length scale of a membrane, $\mathcal{O}\,(\mathrm{cm})$, compared to the tortuous length scale of the the active ($\mathcal{O}\,(\mathrm{nm})$) and supports layers ($\mathcal{O}\,(\mu\mathrm{m})$), respectively. Researchers such as Raeini et al. [2014]; Braga [2016] apply direct numerical simulation to fully resolved porous media from micro-CT scans with the aim of producing relative permeability models. Alternatively to resolving the porous structures, the flow within porous structures can be modeled, with available relative permeability models or without. A resolution approach to the problem is useful for representing ICP and reverse solute transport, but a simultaneous solution with the external flows and their thermo-physical properties adjacent to the membrane surfaces can prove computationally prohibitive.

The authors Horgue et al. [2014] present a generalized framework for modeling multiphase flows in porous media. The particular porous medium is not resolved, but the porosity is merely modeled through the saturation, $S_i = {}^{V_i}/_{V_{void}}$ ($\sum_i S_i = 1$), in the applied transport equations. V_i is the control volume of phase i and V_{void} is the void volume in the porous medium. For the i'th phase, the solute conservation is ensured through equation (1.25).

$$\varepsilon \frac{\partial S_i}{\partial t} + \nabla \cdot \mathbf{U}_i = q_i \tag{1.25}$$

ε is the porosity and q_i is a source or sink term. If no internal sinks or source are present, $q_i = 0$. A modified mass balance equation for a two phase flow is adopted, equation (1.26).

$$\begin{aligned} &\nabla \cdot \left(-\frac{K \cdot \kappa_{r,a}(S_b)}{\mu_a} \cdot (\nabla P_a - \rho_a \mathbf{g}) \right) + \\ &\nabla \cdot \left(-\frac{K \cdot \kappa_{r,b}(S_b)}{\mu_a} \cdot (\nabla P_a - \rho_b \mathbf{g} - \nabla P_c(S_b)) \right) = q_a + q_b \end{aligned} \tag{1.26}$$

This implies that conservation of two species apply, through the sum of q_a (equation (1.27)) and q_b (equation (1.28)).

$$q_a = -\varepsilon \frac{\partial S_b}{\partial t} + \nabla \cdot \left(-\frac{K \cdot \kappa_{r,a}(S_b)}{\mu_a} \cdot (\nabla P_a - \rho_a \mathbf{g}) \right) \tag{1.27}$$

$$q_b = \varepsilon \frac{\partial S_b}{\partial t} + \nabla \cdot \left(-\frac{K \cdot \kappa_{r,b}(S_b)}{\mu_a} \cdot (\nabla P_a - \rho_b \mathbf{g} - \nabla P_c(S_b)) \right) \tag{1.28}$$

Herein, μ_a is the solvent viscosity, $\kappa_{r,i}$ is the permeability, ∇P_a is the phase a pressure gradient, ρ_a the phase density and $\mathbf{g}$ the gravitational acceleration vector. K is the scalar permeability of isotropic permeation, whereas the anisotropic case defines the apparant permeability $\mathbf{K}_i$ as follows,

$$\mathbf{K}_i = \mathbf{K} \cdot \kappa_{r,i}(S_b) \tag{1.29}$$

where $\mathbf{K}$ is the porous medium permeability tensor and $\kappa_{r,i}$ is the relative permeability of phase i. Both anisotropy and isotropy is supported, where for the anisotropic case, $\mathbf{K}$ is defined as a field variable and simply a scalar for isotropic permeability. The relative permeability coefficients are modelled for either liquid or gaseous diffusion, where the published material includes permeability models from the authors Brooks and Corey [1964]; Genuchten [1980]. Furthermore, capillary pressure models are included in the framework, represented by the pressure gradient ∇P_c. In the available capillary model in the framework, $\nabla P_c = \frac{\partial P_c}{\partial S_b} \cdot \nabla S_b$ is a function of the saturation and a

pore size index, through the partial differential gradient. Subsequently, equation (1.26) becomes a Poisson class equation if solved implicitly. However, $\frac{\partial P_c}{\partial S_b}$ is modelled.

From analytical theory, the pressure drop in cylindrical geometries is inversely proportional to the hydraulic diameter and length scale, i.e. the capillary pressure effects are manifested through the included pore size index. The use of the toolbox is originally intended for the permeation of water into oil reservoirs or vice versa, oil into aquifers. The represented physics in the equations above will still apply to other materials, just at a relatively smaller scale and the only necessary change to the framework for repreting the physics in membranes can be changed through the utilized relative permeability model and pore size index.

Novaresio et al. [2011] implement a similar set of transport equations, as Horgue et al. [2014], but applied to a fuel cell with all the relevant components that are found in such an electrochemical converter. The relative permeability coefficients as described above, are modelled by relative permeation models, but with gas diffusion models. This approach to modelling a membrane would be very efficient for modelling PRO, but to the author's knowledge, no relative permeability models for salt and water membrane permeation exist.

1.3.3 Miscellaneous modelling approaches for diffusion and relative permeability modelling

[Zhao et al., 2005] present two neural networks in a deep learning framework, that can predict the solute and solvent mass transfer coefficients ($\mathcal{K}$), that are usually assumed constant in ordinary solution-diffusion models. The two networks are a multilayer perceptron and a normalized radial basis function network, respectively. With the increasing available computational power over the last decade, the applicability of deep learning approaches to various topics in science and technology has grown to being able to represent very complex physical phenomena, mechanisms, etc. The efficiency of this representation is only limited by the fidelity of the data-set, from which a neural network is trained. Training a deep learning algorithm to be able to predict accurately permeability coefficients is possible, but it relies on the availability of several DNS dataset that are based on micro-CT scans of membranes for PRO applications. The potential for applying such methods to CFD in general is significant, but out of the scope of this investigation due to the required amount of time.

1.3.4 Studies in osmotic processes with computational fluid dynamics

CFD for FO is applied by researchers such as Wiley and Fletcher [2002, 2003]; Wardeh and Morvan [2008], but as their frameworks do not include gradients in hydraulic pressure, their permeation models will need modification, similarly to the study of Gruber et al. [2011]. A direct PRO CFD analysis is made by Wang et al. [2016]. In the authors' paper a developed CFD framework for investigating the effects of ECP on the membrane power density at various operating conditions with a lower concentration draw fluid ($\omega_s \leq 3\%$) is presented. For mass and momentum conservation the ordinary transport equations are used along with concentration based advection-diffusion equation:

$$\frac{\partial \rho \mathbf{U} \cdot C}{\partial x} = \frac{\partial}{\partial x}\left(\rho \mathcal{D}_{sw} \frac{\partial C}{\partial x}\right) \tag{1.30}$$

To accommodate closure, permeation model (1.31) is employed. This permeation model, couples the permeation flux with the concentration.

$$C_{F,(m)} = \bar{C}_F \cdot \exp\left(\frac{j_w \cdot \mathcal{S}}{\mathcal{D}_{w_{(m)}}}\right) + \frac{\mathcal{B}}{j_w}\left(C_{D_{(m)}} - C_{F_{(m)}}\right) \cdot \left[\exp\left(\frac{j_w \cdot \mathcal{S}}{\mathcal{D}_{w_{(m)}}}\right) - 1\right] \tag{1.31}$$

$\mathcal{D}_{w_{(m)}}$ is the diffusivity of water incident in the membrane material and $\mathcal{S}$ is the structure parameter, defined as,

$$\mathcal{S} = \frac{t_{sl} \cdot \tau}{\varepsilon} \tag{1.32}$$

Herein, t_{sl} is the porous support thickness and τ is the tortuosity. I.e. through this the microscale flow and the topology of the substructure is modelled through τ, t_{sl} and ε, respectively. The framework is implemented in OpenFOAM, but it is however not published. Considering that the models of these authors and Gruber et al. [2011] are very relevant and applicable to membrane osmotic processes, a study on available membrane permeability models is made in the following.

1.3.5 Selected permeation models

Efforts have gone into formulating accurate permeation models since the first model was formulated by Loeb [1976]. Common to all of them is that they all assume that the driving force on the permeate is comprised of gradients in hydraulic and/or osmotic pressures. Many of them are suitable for studies in reverse and forward osmosis. They vary in complexity depending on assumptions made for simplification. Noteworthy contributions are [Lee et al., 1981; Loeb et al., 1997; Achilli et al., 2009; Xu et al., 2009; Yip et al., 2011; Tiraferri et al., 2013; Touati et al., 2015b; Aschmoneit, 2019]. In this study's developed code, the models of [Loeb et al., 1997; Xu et al., 2009; Touati et al., 2015b; Aschmoneit, 2019] are implemented in the mass flux boundary condition and can all be used. The simplest permeation model [Loeb, 1976], is written as:

$$j_w = \mathcal{A} \cdot \left[\pi_D - \pi_F \ \exp\left(\frac{t}{\mathcal{D}_{sl}}\right) - \Delta P\right] \tag{1.33}$$

This explicit permeation correlation models the osmotic and hydraulic pressure potential and water permeability, and indirectly the effects of membrane topology. However, a large discrepancy is that ICP is neglected through the exclusion of the salt permeability, $\mathcal{B}$. In the model, $\mathcal{D}_{sp}$ is the diffusion coefficient for the support layer, i.e. the magnitude of diffusion in the active layer is not included, and t is the membrane thickness. A more complex formulation is brought forward by Touati et al. [2015b]:

$$\begin{aligned} j_w = {} & \mathcal{A} \cdot \left(\bar{\pi}_D + \frac{\mathcal{B}}{\mathcal{A}} \cdot \left(1 + \frac{\mathcal{A} \cdot \Delta P}{j_w}\right)\right) \cdot \exp\left(-\frac{j_w}{\mathcal{K}_D}\right) \\ & - \left[\bar{\pi}_F + \frac{\mathcal{B}}{\mathcal{A}} \cdot \left(1 + \frac{\mathcal{A} \cdot \Delta P}{j_w}\right)\right] \cdot \exp\left(j_w \cdot \mathcal{R}\right) \cdot \exp\left(\frac{j_w}{\mathcal{K}_F}\right) \cdot \mathcal{A} - \Delta P \cdot \mathcal{A} \end{aligned} \tag{1.34}$$

The nomenclature is as follows: $\mathcal{R}$ is the solute resistivity and $\mathcal{K}_i$ is the mass transfer coefficient of the fluid on either side of the membrane. This means that fluid bulk properties that are dependent on e.g. temperature and salinity, can be inferred in the model. Moreover, like the majority of permeation models, this model is implicit with the water flux j_w occuring on either side of the equality. This necessitates the use of an iterative method for solving for j_w. The implicity occurs when the effects of ICP is included in a permeation model, through $\mathcal{B}$.

1.4 Scope of this study

In this study, the formulation of a widely representable phenomenological permeation model that is not only dependent on hydraulic and osmotic pressures, but furthermore gradients in temperature will be attempted. As through the state of art it can be concluded that it is possible to develop comprehensive models of flows in and around porous media, it is deemed appropriate to implement the formulated permeation model into a CFD framework that uses a non-resolutive approach in modelling the membrane. Furthermore, there is plenty of available literature for thermo-physical properties of saline fluids in various heat and mass transfer, environmental, and chemical engineering journals, so obtaining formulae such as the previous mentioned from Geraldes et al. [2001] is not difficult. Including gradients in temperature, hydraulic pressure and concentration does require a spectrum of coupled transport equations, boundary conditions and thermo-physical formulations. In summary, the complex task warrants:

1. Modelling of scalar and vector transport from
   - *i.* an equation of state with weak compressibility,
   - *ii.* a transport equation of solutes,
   - *iii.* an equation for momentum conservation,
   - *iv.* and an energy equation.

2. Coupling between the feed and draw side through membrane boundary conditions for
   - *i.* convective heat flux,
   - *ii.* solute transport,
   - *iii.* water flux through the formulated permeation model.

3. Implementation of a solver for the governing equations.

Consequently, this report includes the basic underlying theories that have already been presented, utilized numerical methods, applied governing equations to fulfill the list above and simulation results from the developed model. The structure of the report is depicted in figure 1.7.

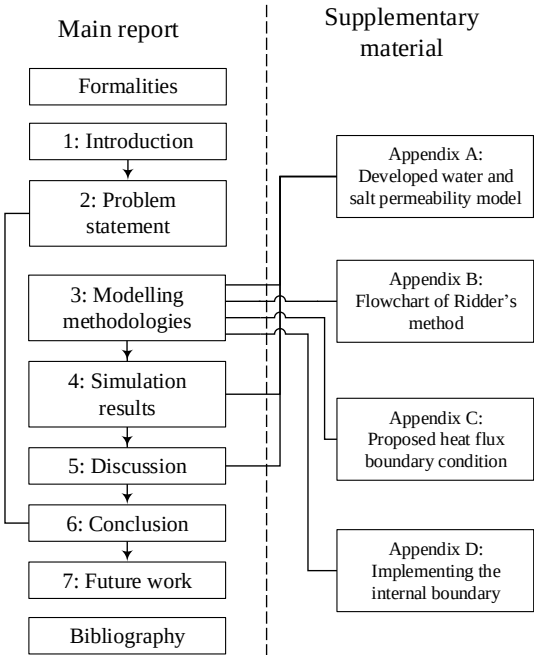

Figure 1.7: Overview of the report structure. The formalities include a titlepage, a preface, a table of contents and a nomenclature.

Problem statement

2

Based on the topics covered in the preceding text, this chapter outlines the objectives of this project.

The main objective of this project is to numerically resolve the permeate boundary layer, on the draw side of a membrane for pressure retarded osmosis, and henceforth be able to estimate the permeation rates dependence on a range of salinities, temperatures and pressures in the draw and feed sides, respectively. For the numerical study the open-source CFD software OpenFOAM® version 4.0 is used to solve the appropriate transport equations. The focus will be on implementing transport of energy in the set of governing equations along with a modified permeation model with temperature dependence. This report is henceforth written to answer the overall problem definition:

> ***How strong is the contribution to the net driving force on the permeate from trans-membrane gradients in pressure, temperature and concentration?***

To form a basis for solving this problem the following research questions will ultimately be answered in this study:

1. Why is it important to investigate thermal effects in relation to the PRO technology?
2. How should the temperature and concentration dependence be formulated into a permeate flux modelling framework, with efficient coupling to thermo-physical properties and all the transport variables including velocity, concentration and temperature?
3. How is such a model implemented into a computational fluid dynamics framework?
4. How does the hydrodynamics in proximity to the membrane govern the membrane permeation performance?

In the following chapter, the numerical case setup is proposed in order to provide opportunity for answering the questions above.

Numerical methodology

3

This chapter introduces the applied numerical methodology in terms of modeling implementations, the case set up, simulation and solution strategies. This will provide the foundation for presenting the simulation results that will be brought forward in the following chapter.

For reproducibility, the following sections aim to outline the procedure for setting up the simulation, and to present which numerical schemes, boundary conditions etc., are used, to realistically represent the flow within a PRO membrane module.

3.1 Case setup and boundary conditions

For prospective validation purposes, the geometry with dimensions depicted in Figure 3.1 is adopted. This geometry is the same used by Touati et al. [2015b], a common geometry utilized in experimental work with PRO (and FO and RO). This geometry deviates significantly from the membranes that are used in commercial PRO applications, mainly in the fact that it is most appropriate to use concentric fibres when large hydraulic pressures are applied.

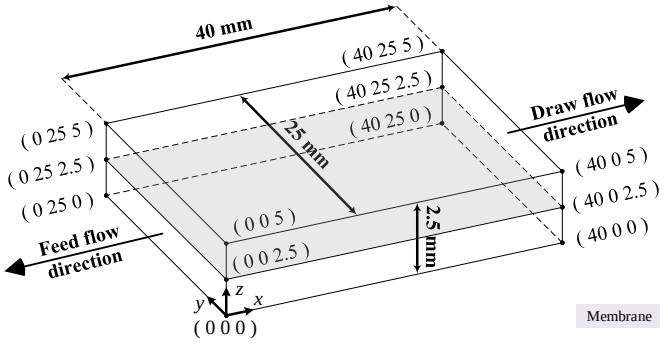

Figure 3.1: Overview of the utilized flat sheet membrane geometry with the draw and feed streams separated by a membrane.

The spatial domain is populated with $30 \times 7 \times 80$ (in the x, y and z directions, respectively) to yield the mesh in Figure 3.2 with 13572 cells. The cells in both channels are distributed with a tanh function with a first cell height of 10^{-6} m $= 1$ μm. The flow directions are orientated in a counter-flow setup.

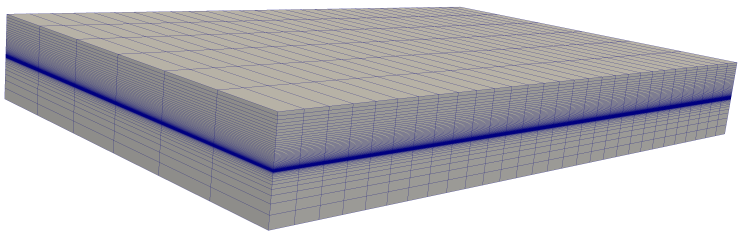

Figure 3.2: Overview of the utilized flat sheet membrane grid.

On the domain faces, the outlined boundary conditions in Tables 3.1 and 3.2 are applied. The boundary conditions for the membrane are presented later in this chapter, as they are more complex than those for the other patches. For the velocity inlets, uniform flow fields cannot be assumed. The Dirichlet condition at the velocity inlets of either stream is a mapped fully developed pipe flow defined by equation (3.1) [Gruber et al., 2011].

$$\mathbf{U} = U_x = 6 \cdot \bar{U} \cdot \frac{z}{h} \cdot \left(1 - \frac{z}{h}\right) \tag{3.1}$$

The boundary conditions for the pressure and velocity fields are summarized in Tables 3.1 and 3.2. Additionally, with known membrane parameters, tangential slip velocities close to the membrane surface can be modelled through equation 1.24 on page 20. However, due to the lack of information about the slip and permeability coefficients for the studied membrane a slip velocity is not imposed.

Table 3.1: Outline of the applied boundary conditions for velocity and pressure. The Dirichlet condition is a fixed value condition.

Face(s)	$\mathbf{U}$	P
Draw inlet	Non-uniform dirichlet condition	$\nabla P = 0$
Draw outlet	$\nabla \mathbf{U} = 0$	Dirichlet condition
Feed inlet	Non-uniform dirichlet condition	$\nabla P = 0$
Feed outlet	$\nabla \mathbf{U} = 0$	Dirichlet condition
Membrane	Equation (3.7)	$\nabla P = 0$
Side walls	Complete slip condition	$\nabla P = 0$
Top and bottom walls	No-slip condition	$\nabla P = 0$

Table 3.2: Outline of the applied boundary conditions for solute mass fraction and temperature.

Face(s)	ω_s	T
Draw inlet	$\nabla \omega_s = 0$	Dirichlet condition
Draw outlet	Dirichlet condition	$\nabla T = 0$
Feed inlet	$\nabla \omega_s = 0$	Dirichlet condition
Feed outlet	Dirichlet condition	$\nabla T = 0$
Membrane	Equation (3.14)	Equations in appendix C
All walls	$\nabla \omega_s = 0$	$\nabla T = 0$

3.2 Simulation and solution strategies

The governing equations, including the primary weakly compressible, momentum and continuity equations and equations for solute and thermal transport are discretized with the finite volume method (FVM) with the open source software OpenFOAM® version 4.0 (OF). The advective and diffusive derivatives in the transport equations are approximated by a central difference scheme which is second order accurate. The pressure is solved for using a preconditioned geometric-algebraic multi-grid (GAMG) conjugate gradient solver whereas the remaining transport properties are solved for with a Gauss-Seidel solver for the subsequent systems of linear equations.

For the solution of pressure, velocity, mass fractions and temperature, a modified version of the guess-and-correct semi-implicit method for pressure-linked equations (SIMPLE) method originally put forward by Patankar and Spalding [1972], is implemented. The modification is the inclusion of solute transport, thermal transport, and variable density. As the flow is assumed laminar, no turbulence model is implemented. Refer to Table 4.1 on page 38 for the Reynolds numbers. To give a brief introduction to how the code in OF is run an overview of the model is essential to present. The general usage of the framework and its simulation procedure, can be represented by Figure 3.3.

The scripts `AllSerial` and `AllrunParallel` initiates the simulations cf. the workflow in the figure, in serial and in parallel, respectively.

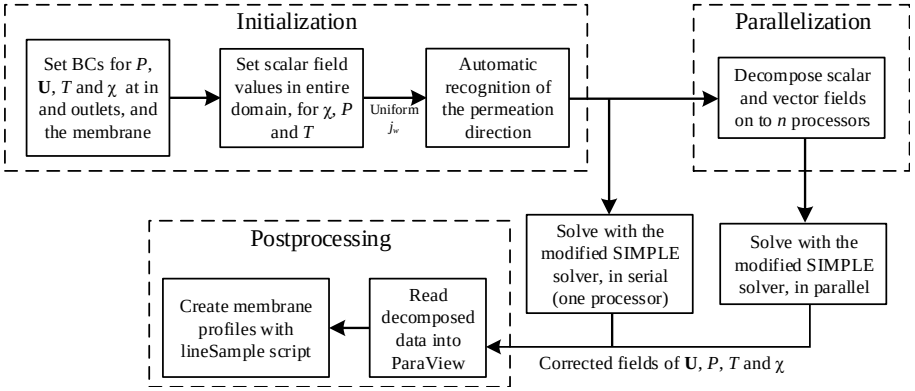

Figure 3.3: Work flow of the model implemented in OpenFOAM®. Default n is 10.

With the general procedure having been presented, an outline of the inferred transport equations and the boundary conditions for the membrane is brought forward. These boundary conditions are coupled with the solution of the transport equations via the modified SIMPLE algorithm.

3.2.1 Implemented transport equations

As the flow is laminar, the effects of transient mechanisms in the flow, are assumed negligible and the transient term $\frac{\partial \phi}{\partial t}$, in all the equations, is excluded in the entire framework.

Mass and momentum conservation, and solute and thermal transport

The flow is weakly compressible due to the working fluid being saline/briny water with the solute mass fraction varying over a large range. Accordingly, the effects of changing density is included in the mass conservation through,

$$\rho \cdot \nabla \mathbf{U} = 0 \tag{3.2}$$

For simplicity, the density is assumed to only vary explicitly with the mass fraction. All of the thermo-physical properties such as density, used in the boundary conditions, and all the transport equations are presented later. For momentum conservation, a diffusion-advection formulation is applied,

$$\nabla \cdot (\rho \mathbf{U} \cdot \mathbf{U}) = -\nabla P + \nabla \cdot (\mu \nabla \mathbf{U}) + \cancel{\rho \mathbf{g}} + \mathrm{S}_{\mathbf{U}} \tag{3.3}$$

As the problem in this study is assumed laminar, turbulence modelling is not applied, and a diffusion-advection formulation will suffice. The pressure gradient is coupled to the velocity through the SIMPLE scheme and the gravitational acceleration can be inferred in the code, but is initially excluded. Species conservation of the salt phase solely is adopted from Gruber et al. [2011] as previously mentioned in the state of the art in chapter 1. The conservation equation is henceforth written as,

$$\nabla \cdot (\rho \mathbf{U} \omega_s) = \nabla \cdot (\rho \mathcal{D}_{ws} \cdot \nabla \omega_s) + \mathrm{S}_{\omega_s} \tag{3.4}$$

The simplest form of the energy equation is used to model heat diffusion and advection:

$$\nabla \left(\rho \mathbf{U} \cdot T\right) = \nabla \left(\alpha \nabla T\right) + \mathrm{S}_T \tag{3.5}$$

where α is the thermal diffusivity. S_i is a source term.

3.2.2 Solution procedure with modified SIMPLE algorithm

The original SIMPLE algorithm is used for a two-way (active) computation of the pressure and velocity fields from the discretized advection-diffusion equations (3.2) and (3.3). The algorithm provides a steady state approximation to the velocity and pressure fields, and their solutions are then sequentially used to passively compute field distributions of solutes and temperature. These scalars are included in the SIMPLE loop and are subsequently solved for at every iteration. They are included in the loop due to the presence of the membrane, for which it is necessary to solve the flux equations for the boundary conditions, (3.7) and (3.14), at every iteration. Cf. the basic formulation of the SIMPLE algorithm, the solution order of the governing equations are as follows:

1. Initialize the scalar and vector fields to provide a guess for $\mathbf{U}, P, \omega_w$ and T.
2. Solve the discretized momentum equations (U_x, U_y, U_z), for corrected velocity components from the initialized pressure field.
3. Solve pressure correction equation to obtain new pressure field.
4. Evaluate the correct pressure and velocity fields from the sum of the corrected fields and the initial fields.
5. Solve the discretized equation for solute transport, ω_s, (3.4).
6. Solve the discretized equation for thermal transport, T, (3.5).

7. Correct fields with the boundary conditions in equations (3.4), (3.7), and (C.1-C.3). The solution procedure for (C.1-C.3) is not yet fully implemented.
8. Return to step 1 if convergence has not been met.

It is noted that at low permeation rates the algorithm is sensitive to relaxation factors, for the mole fraction and velocity, especially. The most essential elements of this framework are the boundary conditions representing the scalar transport through the membrane. Henceforth, the governing equations for this transport will be presented in the following.

3.3 Custom solute, mass flux and slip velocity boundary conditions for the membrane

3.3.1 Boundary condition: temperature, pressure and concentration dependent water permeation flux model

Similarly to the derivation of the idealized hydraulic and osmotic pressure dependent permeation flux equation, $j_w = \mathcal{A}(\Delta\pi - \Delta P)$, a relationship can be formulated with temperature dependence according to the chemical potential contribution from temperature differences, $s_i\ dT$ [Çengel and Boles, 2011]. This contribution then yields the chemical potential change dM_i as follows:

$$dM_i = v_i\ dP - s_i\ dT + \sum_i \left(\frac{\partial M}{\partial \omega_i}\right)_{P,T,\omega_j} d\omega_i \tag{3.6}$$

Following the derivation presented in sections A.2 on page 72 and A.3 on page 75, the inclusion of temperature dependence yields equation (3.7) for the permeation flux.

$$j_w = \mathcal{A} \cdot \left(\left[R\bar{T} \left\{ \chi_{w,0} - \gamma_{w,0} \cdot e_{\Delta T} - e'_{\Delta\pi,\Delta T} \cdot e_{\Delta P} \left(\chi_{w,0} - \gamma_{w,0} \cdot e_{\Delta T} \right) \right\} \right] \cdot \frac{1}{\chi_{w,0} \cdot v_w} \right) \tag{3.7}$$

where the exponential terms are as follows:

$$e_{\Delta T} = \exp\left(\frac{S_w^{\int_t dT}}{R\bar{T}}\right), \qquad S_w^{\int_t dT} = \left| \frac{0.4859}{2} \left(T_t^2 - T_0^2\right) - 133.48 \left(T_t - T_0\right) \right| \tag{3.8}$$

$$e_{\Delta P} = \exp\left(-\frac{\Delta P \cdot v_w}{R\bar{T}}\right) \tag{3.9}$$

$$e'_{\Delta\pi,\Delta T} = \exp\left(v_w \frac{\pi_{D_{(m)}} \cdot \Lambda + \Delta T \cdot R \cdot v_w^{-1}}{R\bar{T}}\right) \tag{3.10}$$

Herein, $\mathcal{A}$ is the ordinary permeability coefficient as in the osmotic and hydraulic pressure dependent flux equation, v_w is the molar specific volume, $S_w^{\int_t dT}$ is the molar entropy (in the code the absolute value is taken, so that heat flux is direction independent), ω is the mass fraction, R is the gas constant, $\bar{T}$ is the bulk temperature $\left(\text{i.e. } \frac{T_0+T_t}{2}\right)$, subscript 0 refers to the surface of the membrane at the draw side and t for the surface at the feed side, χ is the mole fraction, γ is an activity coefficient and $\Delta T = T_t - T_0$. This differential does not impose flux-direction dependence for the heat transfer. The dependence should be modelled through $S_w^{\int_t dT}$. The molar specific

volume is modelled from the mixture density, the solute mass fraction and the molecular weight of water:

$$v_w = \frac{MW_w}{\omega_w \cdot \rho_{mix}} \tag{3.11}$$

Λ is a term that renders the explicit formulation of the flux in equation (3.7), implicit. This is defined according to:

$$\Lambda = \left[\frac{1 - \frac{\chi_{F_{(m)}}}{\chi_{D_{(m)}}} \cdot e_{\mathcal{K}} - e_{\Delta T} \cdot \frac{\gamma_i}{\chi_{D_{(m)}} \cdot j_w} \cdot \mathcal{B}(e_{\mathcal{K}} - 1)}{1 + \frac{\mathcal{B}}{j_w} \cdot (e_{\mathcal{K}} - 1)} \right] \tag{3.12}$$

Herein, $e_{\mathcal{K}} = \exp(j_w \cdot \mathcal{K})$, where $\mathcal{K} = \frac{t_{\text{eff}}}{\mathcal{D}_{\text{eff}}}$ is a membrane specific mass transfer coefficient. The concentration is expressed in terms of mole fraction, and the inlet boundary conditions are expressed in terms of mass fraction. A conversion of the mass fraction field is thus made cf.:

$$\chi_s = \omega_s \cdot \frac{MW_{mix}}{MW_s} \qquad \wedge \qquad \chi_w = 1 - \chi_s$$

Herein, MW is the molecular weight and $_{mix}$ denotes the mixture molecular weight according to:

$$MW_{mix} = \frac{\omega_s \cdot MW_s + \omega_w \cdot MW_w}{\omega_s + \omega_w}, \quad MW_s = 58.4428 \cdot 10^{-3} \quad \wedge \quad MW_w = 18.01528 \cdot 10^{-3} \tag{3.13}$$

3.3.2 Solving the implicit permeation mass flux model

As the permeation model is an implicit formulation an iterative method is implemented to search for appropriate values of j_w, that satisfy the equality in equation 3.7. For this purpose the Ridder's Method for root-finding is applied [Gruber et al., 2011; Ridders, 1979]. A flowchart is found in Figure B.1 on page 79. A simplified outline of the method can describe its implementation in the following steps:

1. Initialize the algorithm with lower and upper bounds for the flux j_w at the right hand side (RHS) of equation (3.7), i.e. in Λ and evaluate j_w on the left hand side from the average of the two RHS bounds.
2. Enter a for-loop that at each iteration computes weighted fluxes within the bounds and chooses a new flux via a comparison logic.
3. During the iterative process, convergence between the LHS and RHS of equation (3.7) is monitored to ensure that the difference between them is below the predefined accuracy.
4. Return the latest update of j_w from the iterated RHS flux.

The convergence in the transport properties of the whole framework is heavily dependent on the stability of the permeation equation, as it couples thermo-physical properties, species concentration, pressure and temperature. Consider the realistic orders of magnitude of the transport properties, as listed below in order of increasing magnitude,

$$\mathcal{O}(\mathbf{U}) = [10^{-2}, 10^{-1}], \quad \mathcal{O}(U_z) \sim 10^{-6} \text{ (for membrane-normal permeation)}$$
$$\mathcal{O}(\chi) = [10^{-3}, 10^{-2}]$$
$$\mathcal{O}(T) = 10^2$$
$$\mathcal{O}(\rho) = 10^3$$
$$\mathcal{O}(P) = [10^5, 10^6]$$

The extremities are contained within the velocities and the hydraulic pressure. From parametric studies it is found that the iterative method is sensitive to the magnitude of local velocities and mole fractions. Transitioning from the mole fraction magnitude of 10^{-2} to 10^{-3} causes divergence, for which the algorithm is programmed to return $j_w = 0$. At lower solute concentrations, MW_{mix} approaches MW_w which means that $\chi_s = \omega_s \frac{MW_w}{MW_s} \sim \omega_s \cdot 0.3$. I.e. at $\omega_s \simeq 3\%$, the molefraction is approximately 1%. It is duly noted that $\mathbf{U}$ is not directly implemented in the permeation equation. The permeation flux alters the cross flow velocities within the boundary layer (leading to ECP).

3.3.3 Boundary condition: reverse solute flux

For species transport across the membrane, equation (3.14) [Lee et al., 1981], is applied so as to satisfy the prescribed solute balance.

$$j_s = -\rho_{mix}\mathcal{D}_{ws} \cdot \frac{\partial \omega_w}{\partial \mathbf{n}} + \rho_{mix}\omega_{w_{(m)}} \cdot j_w \tag{3.14}$$

This is implemented in OF as a boundary condition that updates the mass fraction of the cells adjacent to the membrane surface according to the obtained permeate flux from equation (3.7) and the linear relationship [Gruber et al., 2011],

$$j_s = \frac{\mathcal{B}}{\varphi \cdot \mathcal{A}} \cdot j_w \tag{3.15}$$

No modification is made to this boundary condition. However, as energy transport is included in the system of transport and conservation equations, a boundary condition for heat flux is needed.

3.3.4 Boundary condition: thermal transport

The heat flux equations, presented in appendix C on page 81, are implemented in the OF source code, but further development of the boundary condition is needed as the cells on either side of the membrane need to have their internal coefficients updated with the predicted temperatures from these equations. This manipulation is done on the coefficient matrix A of the system of linear equations, from the discretization of the governing transport and conservation equations, $[A] \cdot [\Phi] = [b]$. This development is left as future work which leaves the problem not to be polarized by the temperature, in the cells adjacent to the membrane. Nevertheless, the differential temperature in equations (3.8) and (3.10) still alters the permeate flux.

3.3.5 Inferral of slip velocities

An important implementation in the framework is the modelling of the magnitude of the slip velocities, incident at the surface of the membrane. The slip velocity computation is implemented in the mass transfer boundary condition. Directly manipulating the surface-parallel velocities changes the height of the boundary layer, from a redistribution of the momentum flux. This in response changes the permeation rate due to the displacement of the concentration profile in the membrane surface-normal direction [Geankoplis, 2003]. In the code, equation (3.16) is directly applied to manipulate the first cell layer in the matrix for the vector field, adjacent to the membrane surface on the draw side.

$$U_{\text{slip}} = -\frac{\sqrt{\kappa}}{\zeta} \cdot \frac{\partial \mathbf{U}}{\partial \mathbf{n}} \tag{3.16}$$

The magnitude of the proportionality coefficient $-\frac{\sqrt{\kappa}}{\zeta}$ is determined by the surface roughness, porosity and structure of the membrane and subsequently has a large variance, as many membranes are different in topology.

3.4 Utilized thermophysical properties

In the permeation model and for the thermophysical properties in the SIMPLE scheme, a range of explicit correlations is used. To simplify the procedure, each property is only dependent on one variable, either mass fraction or temperature, depending on which shows stronger dependence with the property. Consider e.g. the partial molar entropy of water with dependence on salinity and temperature, seen in Figure 5.4. Over the range $\omega_s \in [2\%, 12\%]$, the entropy exhibits a strong dependence on temperature, but in comparison, a lesser dependence on salinity. For simplicity the entropy is modelled explicitly as a function of only temperature, as multi-variable equations of state are relatively complex. To formulate a correlation, an intermediate concentration of 8% is chosen yielding the polynomial fit:

$$s_w = -0.0007 \cdot T^2 + 0.927 \cdot T - 200.05 \tag{3.17}$$

This equation is integrated from 0 to the membrane thickness t as described in section A.2 on page 72 to yield the temperature dependent absolute entropy:

$$S_w^{\int_t dT} = \left| \frac{0.4859}{2} \left(T_t^2 - T_0^2 \right) - 133.48 \left(T_t - T_0 \right) \right| \tag{3.18}$$

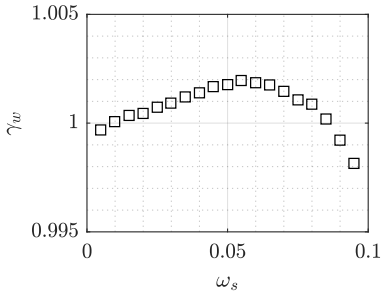

Figure 3.4: Dependence of the water activity coefficient on the concentration of salt in a one-component sodium chloride aqueous mixture computed by Miyawaki et al. [1997].

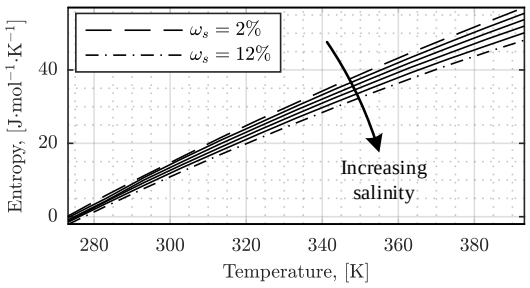

Figure 3.5: The dependence of entropy of temperature and the mass fraction of salt [Sharqawy et al., 2010].

In equations (3.7) and (3.12) activity coefficients are implemented to represent the thermodynamic deviation in the microscopic interactions between solute and solvent from an ideal behaviour. This factor is modelled from experimental results [Miyawaki et al., 1997],

$$\gamma_w = -19.224 \cdot \omega_s^3 + 1.5192 \cdot \omega_s^2 + 0.0137 \cdot \omega_s + 0.9997 \tag{3.19}$$

Simulation results

4

This chapter aims to present in detail the case setup for the flat sheet membrane and a sensitivity analysis of the respective parameters in the permeation model. The sensitivity analysis is performed with the aim to identify discrepancies and tendencies that render the model partially unrealistic.

Given the complexity of the developed permeation model and its susceptibility to heavy flux variation from values of the parameters that constitutes its stability, a thorough sensitivity analysis is performed. The main aim of the analysis is to identify the more dominant terms in the model that define j_w and that induce floating point and rounding errors. These errors do arise with the permeate flux having an order of magnitude that varies in the range of $[10^{-5}, 10^{-9}]$. Initially, a benchmark simulation and its case setup will be presented. The benchmark results will be the basis for a comparison of the various terms' effect on the predicted permeation flux.

4.1 Benchmark simulation

The benchmark simulation will be based on simulation results from Touati et al. [2015b], that eventually can be used as a means of validation of the present solver. The case is isothermal and setup with the same values for thermo-physical properties as reported in the article. In the following, values for these will be outlined. The considered geometry is the one depicted in Figure 3.1 on page 29.

4.1.1 Applied boundary conditions, membrane properties, and thermo-physical properties

Dirichlet conditioned values for the transport properties are summarized in Table 4.1. The given inlet mean velocities correspond to a volumetric flowrate of 50 $\frac{\text{mL}}{\text{min}}$. This flow rate is the primary value used in the study of Touati et al. [2015b]. The permeation flux is however not expected to vary with the feed side flow rate, unless $\mathcal{O}(J_w) \sim \mathcal{O}\left(\dot{V}_{F,in}\right)$ [Kimura and Sourirajan, 1967], where J_w is the total membrane volumetric permeation. The inlet Reynolds numbers are calculated cf.:

$$Re_{D_h} = \frac{|\mathbf{U}| \cdot D_h}{\nu} \tag{4.1}$$

The kinematic viscosity is computed from equations (1.18) and (1.20), according to the solute mass fraction. The hydraulic diameter is calculated as:

$$D_h = \frac{2 \cdot \Delta y \cdot \Delta z}{\Delta y + \Delta z} = 0.00455 \tag{4.2}$$

An intermediate differential pressure ($\Delta P = 23.8$ bar) is chosen for the bench-line and a brackish equivalent salinity is chosen, yielding a draw side solute mass fraction of 6% and a feed side solute mass fraction of 0.05%. An isothermal case is considered with a temperature of 293.15 K.

Table 4.1: Benchmark Dirichlet-condition values for the sensitivity analysis. Zero-gradient is abbreviated ZG. The velocity value is the average of the mapped velocities in the fully developed distribution in equation (3.1). 0.0133 $^{\mathrm{m}}/_{\mathrm{s}}$ corresponds to 50 $^{\mathrm{mL}}/_{\mathrm{min}}$.

	$\lvert\mathbf{U}\rvert$	Re_{D_h}	$P \times 10^{-5}$	ω_s	T
Draw inlet	0.0133	64.3	ZG	6%	293.15
Draw outlet	ZG	$\propto j_w$	25.8	ZG	ZG
Feed inlet	0.0133	66.2	ZG	0.05%	293.15
Feed outlet	ZG	$\propto j_w^{-1}$	2	ZG	ZG

For the benchmark simulation the thermo-physical properties are defined according to Table 4.2. R is the gas constant for water and α is the thermal diffusivity. Presently, the thermal boundary condition for heat flux is not fully implemented. This means that both streams will have invariant cross-sectional temperature profiles, and that the temperature profiles on either side of the membrane are non-polarized, i.e. uniform. Due to this, the thermal diffusivity has no effect on the membrane diffusion until the boundary condition is implemented.

Table 4.2: Utilized values and correlations for thermo-physical properties, for the simulations. $t_{\mathrm{eff}} = t_{al} + t_{sl}$.

Thermo-physical property	v_w	$S_w^{\int_t dT}$	R	MW_{mix}
Value/correlation	Eq. (3.11)	Eq. (3.17)	8.3145	Eq. (3.13)

α	ρ_{mix}	$\mathcal{D}_{sw}$	μ	γ_w
$1.46 \cdot 10^{-7}$	Eq. (1.20)	Eq. (1.19)	Eq. (1.18)	Eq. (3.19)

The parameters used for modelling the membrane are summarized in Table 4.3. In the paper by Touati et al. [2015b] constant permeability coefficients for water and salt are used. The same values are used in the benchmark simulation. The thicknesses of the active and support layers t_{al} and t_{sl}, correspond to the configuration of the same IGB membrane Touati et al. use in their experiments. A no-slip condition at the membrane surfaces is applied, i.e. $-\frac{\sqrt{\kappa}}{\zeta} = 0$. †The membrane diffusivity is calculated from the benchmark permeability coefficient $\mathcal{A}$ assuming a sorption coefficient value of $K_w = 1$:

$$\mathcal{D}_{(m)} = \frac{\mathcal{A} \cdot t_{\mathrm{eff}} \cdot R \cdot \bar{T}}{K_w \cdot \chi_{w,0} \cdot v_w}$$

The mass transfer coefficient is defined from this diffusivity,

$$\mathcal{K} = \frac{t_{\mathrm{eff}}}{\mathcal{D}_{(m)}}$$

h_{al} and h_{sl} are used in the thermal boundary condition. This outlines the settings for the benchmark simulation and henceforth the results from this are presented in the following.

Table 4.3: Membrane specific properties used in the simulations.

Membrane property	$\mathcal{A}$	$\mathcal{B}$	t_{al}	t_{sl}	$-\frac{\sqrt{\kappa}}{\zeta}$
Value/correlation	$1.06 \cdot 10^{-12}$	$2.62 \cdot 10^{-8}$	$100 \cdot 10^{-9}$	$12 \cdot 10^{-6}$	0

h_{al}	h_{sl}	$\mathcal{K}$	$\mathcal{D}_{(m)}$
4806	3966	2617.9	$^{\dagger}1.764 \cdot 10^{-9}$

4.1.2 Benchmark simulation result

The benchmark result yields a power density of $PD = 0.27\ \frac{\mathrm{W}}{\mathrm{m}^2}$ as compared to the power density reported by Touati et al. [2015b] of $PD \sim 5.5\ \frac{\mathrm{W}}{\mathrm{m}^2}$. The sensitivity analysis aims to identify the reason for the deviation between these. The permeation flux is predicted to $j_w = 1.12 \cdot 10^{-7}\ \frac{\mathrm{m}^3}{\mathrm{m}^2 \cdot \mathrm{s}} = 0.404\ \frac{\mathrm{L}}{\mathrm{m}^2 \cdot \mathrm{hr}}$. The maximum performance coincide with the $\Delta P = \frac{1}{2}\Delta\pi = 23.8$ bar, as expected. A polynomial progression with pressure is also expected for the developed model. The setup for this benchmark simulation will be used as a reference for the sensitivity analysis.

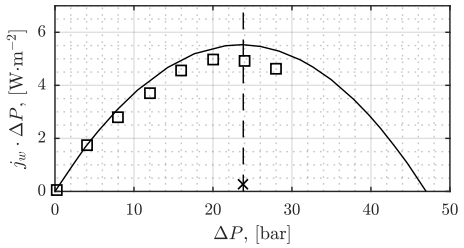

Figure 4.1: Power density as a function of hydraulic pressure difference.
$\times$ − present model, $j_w = 1.12 \cdot 10^{-7}\ \frac{\mathrm{m}^3}{\mathrm{m}^2 \cdot \mathrm{s}} = 0.404\ \frac{\mathrm{L}}{\mathrm{m}^2 \cdot \mathrm{hr}} \rightarrow PD = j_w \cdot \Delta P = 0.27$.
solid line − simulation results from Touati et al. [2015b].
□ − experimental results from Touati et al. [2015b].
dashed line − $\pi_D/2$.

4.2 Sensitivity analysis

4.2.1 Variation of the parameter-space for the implicit permeation model

To investigate the nature of the various terms in the developed model, a sensitivity analysis will be made for each term, with the benchmark simulation as a reference. Each parameter is varied separately with all the other remaining parameters held constant at the benchmark reference values. A total of 12 properties will be varied in the test matrix presented in the following. Moreover, the flow rates across the membranes will be varied to analyze the cross-flow momentum dependence.

Test matrix

1. $\mathcal{K} = f(K_w)$
2. ΔT
3. $\bar{T}$
4. ΔP
5. v_w
6. $\pi_{D_{(m)}}$
7. $\Delta\pi$
8. $\pi_{F_{(m)}}$
9. γ_i
10. $\mathcal{B}$
11. $\mathcal{A}$
12. $\gamma_{w,0}$

The ranges within which these vary, are specified in Table 4.4. Both a realistic range of values and one or two extremetie(s) are investigated. The mass transfer coefficient is a function of the water

sorption coefficient, K_w, in the membrane, $\mathcal{K} = \frac{t_{\text{eff}}}{\mathcal{D}_{\text{eff}}}$:

$$\mathcal{K} = \frac{t_{\text{eff}}}{\mathcal{D}_{\text{eff}}} = \frac{\cancel{t_{\text{eff}}} \cdot K_w \cdot \chi_{w,0} \cdot v_w}{\mathcal{A} \cdot \cancel{t_{\text{eff}}} \cdot R \cdot \bar{T}} = \frac{K_w \cdot \chi_{w,0} \cdot v_w}{\mathcal{A} \cdot R \cdot \bar{T}} \tag{4.3}$$

The remaining variables have already been defined in the preceding text.

Table 4.4: Outline of the properties that is varied in the sensitivity analysis.

Model term	Property	Realistic value range, extremeties
$e_{\mathcal{K}}$	K_w	$[0.4, 1]$
	$\mathcal{K}$	$[2617.9, 3272.4]$ $\{10^{-2}, 13 \cdot 10^3\}$
$e_{\Delta T}$	$S_w^{\int_t dT}(\Delta T)$	$[0, 30]$
	$\bar{T}$	$[283.15, 363.15]$ $\{273.15, 373.15\}$
$e_{\Delta P}$	ΔP	$[0, 47.7] \cdot 10^5$
	v_w	$[1.807, 1.982] \cdot 10^{-5}$ $\{2 \cdot 10^{-6}, 2 \cdot 10^{-4}\}$
	$\bar{T}$	$[283.15, 363.15]$ $\{273.15, 373.15\}$
$e'_{\Delta\pi,\Delta T}$	v_w	$[1.807, 1.982] \cdot 10^{-5}$ $\{2 \cdot 10^{-6}, 2 \cdot 10^{-4}\}$
	$\pi_{D_{(m)}}$	$[0, 146] \cdot 10^5$
	ΔT	$[0, 30]$
	$\bar{T}$	$[283.15, 363.15]$ $\{273.15, 373.15\}$
Λ	$\Delta\pi$	$[23.8, 146] \cdot 10^5$
	$\pi_{F_{(m)}}$	$[2.24, 20.1] \cdot 10^5$
	γ_i	$[0.5, 1.25]$ $\{0.01, 5\}$
	$\mathcal{B}$	$[1.764, 3.110] \cdot 10^{-8}$ $\{10^{-14}, 10^{-7}\}$
	$\mathcal{A}$	$[1.060, 2.004] \cdot 10^{-12}$ $\{10^{-13}, 5 \cdot 10^{-11}\}$
Permeation equation (3.7)	$\gamma_{w,0}$	$[0.995, 1.5]$ $\{5\}$
	$\bar{T}$	$[283.15, 363.15]$ $\{273.15, 373.15\}$
	v_w	$[1.807, 1.982] \cdot 10^{-5}$ $\{2 \cdot 10^{-6}, 2 \cdot 10^{-4}\}$

Sensitivity analysis simulation results

Figure 4.2 shows the predicted values for the permeation flux (left second axis) and power densities (right second axis) for the parameters listed in Table 4.4, excluding the simulated extreme values. The fluxes and power densities for these extremeties are depicted in Figure 4.4 along with the realistic values.

The mass transfer coefficient is a multi-variable parameter that is very specific for the particular membrane being modelled. Given that it represents membrane geometry, diffusivity, chemical potentials etc. its significance in the predicted permeation rate should be predominant. Considering Figures 4.2 and 4.4 (a) it is evident that the model is insensitive to the mass transfer exponential, $\exp(j_w \cdot \mathcal{K})$. It should in reality be that j_w is more sensitive to $\mathcal{K}$, $\mathcal{A}$ and $\mathcal{B}$, so in prospective analyses of this study attention should be brought to applying weights to these for more appropriate inter-dependence. $\mathcal{K}$ produces reliable and stable results within the range of $\sim [0.01, 1.3 \cdot 10^4]$. On either side of the limits, the model diverges. $\mathcal{K} = 1.3 \cdot 10^4$ corresponds to the value of the mass transfer exponential $e_{\mathcal{K}} = 1.00146$ with $j_w = 1.12787 \cdot 10^{-7}$ $\text{m}^3 \cdot \text{s}^{-1}$. It is not known if the exponential has a larger effect at high permeation rates.

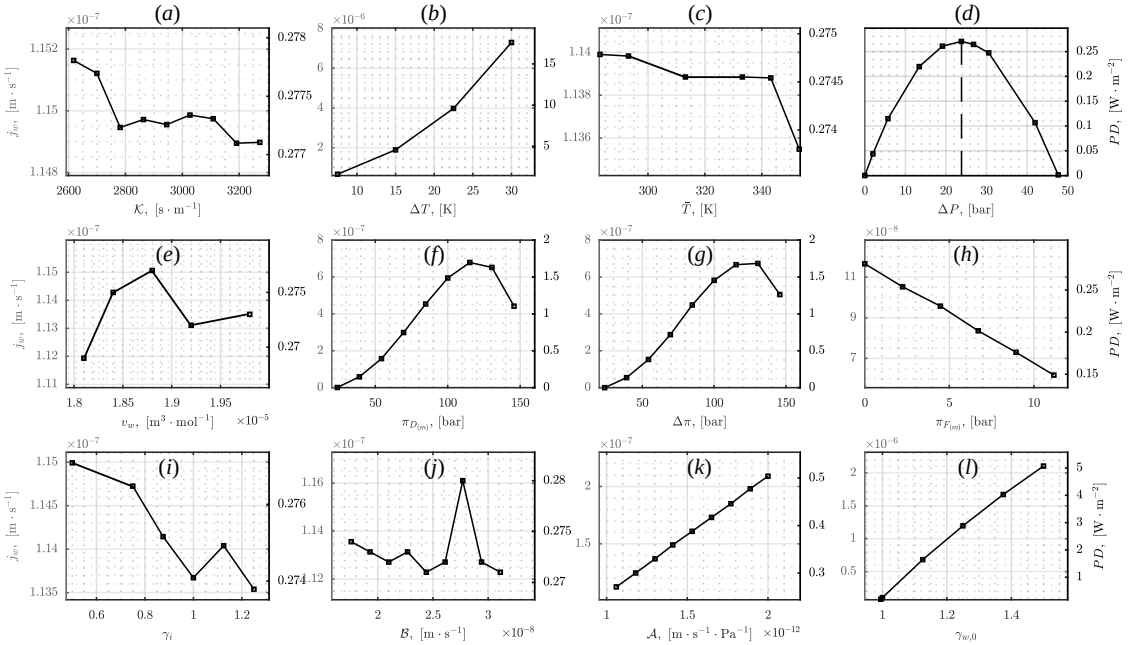

Figure 4.2: Sensitivity analysis on the permeation flux j_w and power density PD. The ranges that each parameter is defined by are physically realistic in comparison to the values given in Touati et al. [2015b].

The effect the temperature gradient over a porous material has on the permeate mass flux is in literature referred to as the Soret effect [Phattaranawik and Jiraratananon, 2001; Rahman and Saghir, 2014; Banat and Simandl, 1994]. The temperature gradient is modelled through ΔT in the exponentials $e_{\Delta T}$ and $e^{'}_{\Delta\pi,\Delta T}$ so that $\Delta T = 0$ infers no change to the permeation rate. The $e_{\Delta T}$ exponential as a function of the temperature gradient is depicted in Figure 4.3 (left). As the gradient in reality might not be more than $\Delta T = 60$ the value of the exponential, with respect to exp(0), does not change more than 39% for $\Delta T \leq 60$. But considering that this difference is in the same order of magnitude as for $\gamma_{w,0}$, which is multiplied by both the exponential terms $e_{\Delta T}$ in equation (3.7), the exponential is expected to have the same effect as from varying $\gamma_{w,0}$. In the exponential $e^{'}_{\Delta\pi,\Delta T}$ the contribution from the temperature gradient, excluding the potential from osmotic pressure, is $\exp\left(\frac{\Delta T \cdot \cancel{R}}{\bar{T} \cdot \cancel{R}}\right)$. The value of the contribution is depicted in Figure 4.3 (right). I.e. the exponential value increases up to 22% at $\Delta T = 60$, so the temperature gradient is more predominant in $e_{\Delta T}$. The exponential $e^{'}_{\Delta\pi,\Delta T}$ is offset by $\left(\frac{v_w \cdot \pi_{D_{(m)}} \cdot \Lambda}{R\bar{T}}\right)$. For the reference simulation the order of magnitude of Λ is $\mathcal{O}(\Lambda) = 10^0$ which yields the order of magnitude $\mathcal{O}\left(\frac{v_w \cdot \pi_{D_{(m)}} \cdot \Lambda}{R\bar{T}}\right) = 10^{-3}$ for the ratio. I.e. the ratios should be balanced to yield appropriate contributions from the driving force from osmotic pressure and the Soret effect.

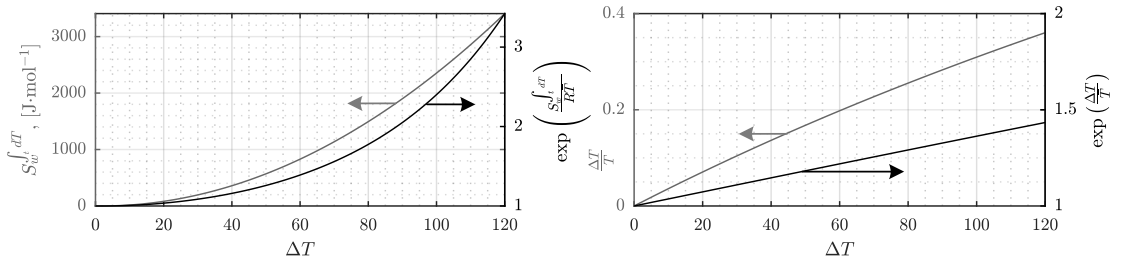

Figure 4.3: Value of equation (A.21) and its corresponding exponential value as a function of the temperature gradient. At $\Delta T = 0$, $\bar{T} = T_D = T_F = 293.15$ K.

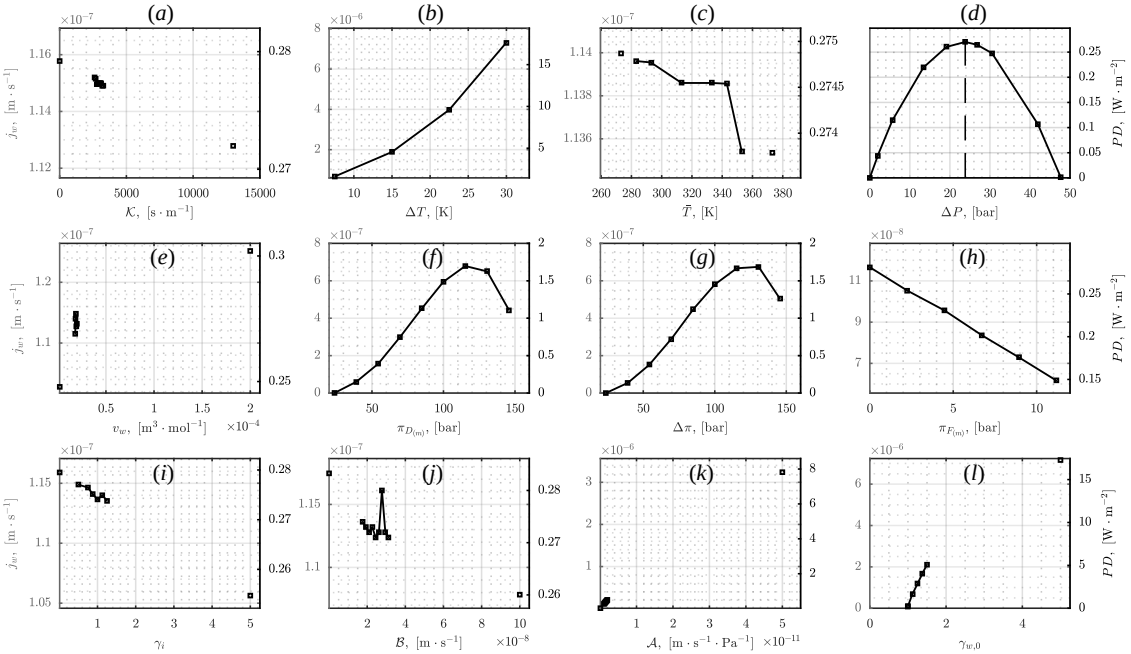

Figure 4.4: Sensitivity analysis on the permeation flux j_w and power density PD. The ranges that each parameter is defined by are chosen to be unrealistic with the aim of validating the results from Touati et al. [2015b].

The bulk temperature is varied coherently in both streams assuming an isothermal condition so that $\bar{T} = \bar{T}_D = \bar{T}_F$. Cf. the fact that the permeability increases with the bulk temperature, as has been previously discussed in this report, it is expected that j_w increases with the bulk temperature. This is, however, not the case as is evident from Figures 4.2 and 4.4 where the effect is opposite. If this is only a tendency that applies to the inherently low permeation rates, the temperature dependence should be investigated at realistic power densities by e.g. increasing $\gamma_{w,0}$. Otherwise the dependence should be explicitly altered by taking the reciprocal of $\bar{T}$ where it is appropriate. But it is now evident that there in the model is direct implication in the predicted permeation rate from gradients in hydraulic pressure, osmotic pressure and temperature, and moreover the bulk temperature distribution.

The effect mechanical driving forces such as external hydraulic pressure and osmotic pressure from solute concentration infer, is attributed to the Dufour effect [Phattaranawik and Jiraratananon, 2001]. In combination with the Soret effect several complex mechanisms constitute the inherently non-linear trans-membrane energy flux. As is depicted in Figures 4.2 and 4.4, the energy flux assumes a polynomial regression as can be expected from the theory described in section 1.3 on page 16. This theory states that the energy flux will maximize at $\Delta P = \frac{1}{2}\Delta\pi$ (indicated by the dashed line) but this is assuming that the Soret effect and thermal effects from the bulk temperature distribution are negligible. As a consequence the energy maximum should be shifted relative to this theoretical maximum because of thermal effects. This does not occur in the results due to the insensitivity to $\bar{T}$.

The molar specific volume is a parameter that does not have a lot of variance as it is exclusively defined by the salinity as seen in Figure 4.5. I.e. the limits of this parameter are very well defined within the plotted extremes and the values in Figure 4.4 are not attainable.

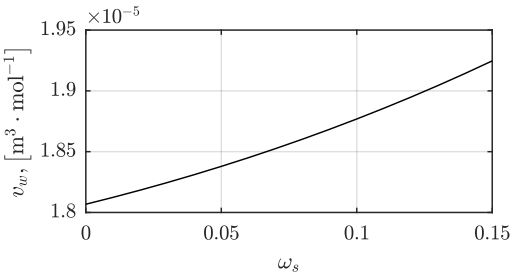

Figure 4.5: Molar specific volume as a function of solute mass fraction.

$\pi_{D_{(m)}}$ is varied over the prescribed range but with a uniform distribution of values in every cell adjacent to the membrane surface. This constitutes an ideal membrane permeation process with no ECP. The power density and membrane mass flux is depicted in Figures 4.2 and 4.4 (f). As expected, the energy flux through the membrane becomes zero when $\Delta\pi \rightarrow \Delta P$. With increasing osmotic pressures the flux undergoes a non-linear growth until it saturates at approximately 115 bar after which it decreases. Above $\Delta\pi = 146$ bar the solution diverges.

$\Delta\pi$ is simulated by varying the saline concentration over the same range as for $\pi_{D_{(m)}}$ at the draw inlet whilst retaining a constant concentration in the feed stream. Contrary to the variation in $\pi_{D_{(m)}}$, these simulations include ECP. The variation in $\Delta\pi$ yields the progression in the permeation rate seen in Figures 4.2 and 4.4 (g). This does not appear to assume a polynomial shape which is due to its direct influence on the permeation equation (3.7), Λ and the exponential $e^{'}_{\Delta\pi,\Delta T}$ via the variables $v_w, \pi_{D_{(m)}}, \gamma_{w,0}$ and $\chi_{D_{(m)}}$. The solution given by the permeation model produces a floating point error when $\Delta\pi \rightarrow \Delta P$ and similarly for all $\omega_s > 18\%$ which corresponds to $\Delta\pi = 146$ bar. In figure 4.6 the data in Figures 4.2 and 4.4 (f,g) are compared. It is seen that for pressures between the zero-flux pressure and the pressure yielding the maximum power density, the ideal profile consistently produces a marginally higher energy flux with a maximum deviation of approximately 8%. Above $\Delta\pi = 146$ bar, the effect reverses and ECP becomes beneficial to the energy flux with a deviation of 14%.

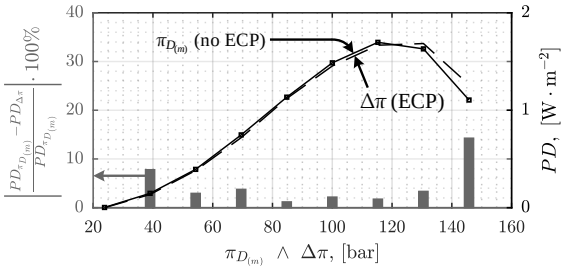

Figure 4.6: Comparison of power densities achieved with and without concentration polarization. Bars indicate percentiles (left hand side second axis) in deviations between the power densities, the dashed line is the power density with ECP and the solid line without.

The concentration at the membrane surface $\pi_{F_{(m)}}$ on the feed side is varied by varying the inlet concentration. This is valid assuming that no C-ECP occurs. The results from the simulations show that the permeation performance is highly susceptible to the concentration in the feed stream. This is due to the direct effects the salinity has on the extent of ICP. This finding is also supported by other researchers in the field including Touati et al. [2015b]. A salt mass fraction in the feed solution as low as 1.1% leads to a degradation in the power density of 36.6% compared to a virtually pure solution (simulated as $\omega_s = 10^{-6}$). This proves the models ability to model ICP.

Similarly for the activity coefficient for the dilute solution inside the membrane porous support, γ_i, traditional values given for the molecular interaction in free-shear flow might not apply to the microscopic flow structures that can be affected by the porous topology of the support layer. However, the model is insensitive to this parameter and the value of the parameter is pending further investigation.

$\mathcal{B}$ decays up until $\mathcal{B} \simeq 2.2 \cdot 10^{-8}$ after which the solution becomes unstable. Considering that the permeation rate is close to the magnitude of machine precision, it is likely that round-off errors cause the fluctuating profiles. From a physical interpretation, the permeation flux is inverse proportional to the salt permeability, as the percolation of solutes increases the internal concentration polarization. I.e. it is expected that the permeation rate is mitigated with an increasing solute permeability.

As the permeability coefficient $\mathcal{A}$ is a scaling constant applied only to equation (3.7), j_w is expected to vary linearly with $\mathcal{A}$. As is confirmed in the figure, this is the case for $\mathcal{A}$. Moreover, the results confirms the robustness of the numerical schemes implemented in this framework such as Ridder's method for root-finding. To achieve realistic values for the power density, the coefficient should increase by one order of magnitude. If this is realistic depends on which membrane is used. High performance membranes might be able to accommodate such permeability coefficients, but given that this analysis is based on the specific membrane used by Touati et al. [2015b], the variation of an order of magnitude is not justifiable.

The water activity coefficient $\gamma_{w,0}$ directly scales the exponentials constituted by the chemical potentials from gradients in pressure, temperature and concentration and it is henceforth expected that the permeation rate is strongly dependent on the coefficient. Figures 4.2 and 4.4 show that this assumption applies. As a consequence, the value of the coefficient ought to be chosen with

attention to the actual hydrodynamics that govern the flow adjacent to the membrane. Figure 4.7 depicts a stream-wise cross section of the membrane module from the simulation with $\gamma_{w,0} = 1.5$ showing the concentration profiles in the draw and feed streams.

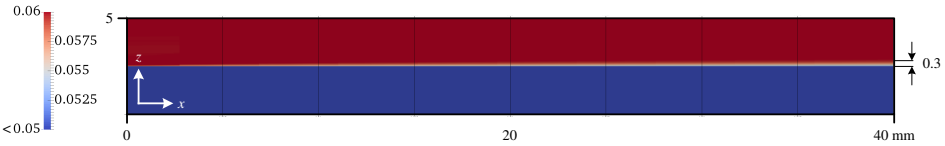

Figure 4.7: x-z cross sectional contour of χ_s. Benchmark simulation with $\gamma_{w,0} = 1.5$. $PD = 5.1$. The height of the boundary layer is approximately 0.3 mm or 12% of the draw channel height.

Figure 4.8 shows the same profile situated in the module with the membrane-normal velocity component contour u_z and the midpoint cross sectional velocity profiles. The latter velocity profiles are scaled to 10% and then normalized by the average of the inlet velocity. With this activity coefficient a power density of $PD = 5.1$ is achieved. Considering that a power density of $PD = 5$ is considered the minimum economically viable performance [Ramon et al., 2011], the amount of dilution and the permeation rate attained in this simulation are assumed realistic.

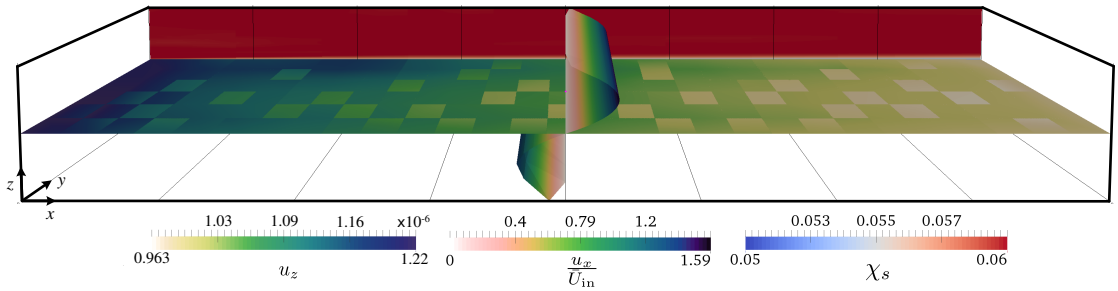

Figure 4.8: Contours of the membrane-normal velocities, stream-wise normalized velocity profiles and salt mass fraction.

The height of the diluted boundary layer is approximately 0.3 mm corresponding to 12% of the draw channel height. Within this boundary layer the draw stream is only diluted from a mass fraction of 6% to 5% which constitutes a minor fraction of the total Gibb's free energy. I.e. if the entire potential of the salt gradient is to be utilized the membrane module should be significantly longer. Qualitatively this agrees with the dimensions of conventional hollow fibre membranes. In hollow fibres used in commercial applications the magnitude of the dimensions of the draw and feed channels are in the order of 100 μm = 1 mm. The length of a fibre is around 1 m which can accommodate a more extensive dilution and a permeation volumetric flow that is comparable to the flow-rate at the draw inlet.

4.2.2 Variation of the cross flow velocities

Not only the membrane parameters are defining for the permeation flux, but so is the momentum transfer between the freestream and the boundary layer. Increasing the momentum flux in the boundary layer decreases the residence times of the particles which causes the boundary layer to decrease in thickness. This displaces the concentration distribution in the boundary layer closer to the membrane surface, which augments the osmotic forces produced by the altered concentration gradients. Table 4.5 and Figure 4.9 outlines simulation results with the benchmark case setup where $\gamma_{w,0} = 1.5$ to avoid floating point errors. As expected, and as is evident from the figure, the energy flux is enhanced with higher cross flow velocities.

Table 4.5: Variation of the draw inlet velocity and the attained power densities.

	Min, max	Residence time $\left(\frac{L}{\bar{U}_{D,\text{in}}}\right)$	PD	$\left(\frac{PD_{\max}-PD_{\min}}{PD_{\max}} \cdot 100\%\right)$
$\lvert\bar{U}_{D,\text{in}}\rvert$	{0.005, 0.08}	{8, 0.66}	{4.72, 5.50}	14.1%

The largest enhancement of the power density is 14.1%. This substantiates the importance of applying the previously mentioned slip condition achievable by equation (1.24). At lower velocities the diffusive term in the momentum equations is comparable to the advective term in magnitude resulting in the permeate being distributed more effectively in the membrane surface-normal direction.

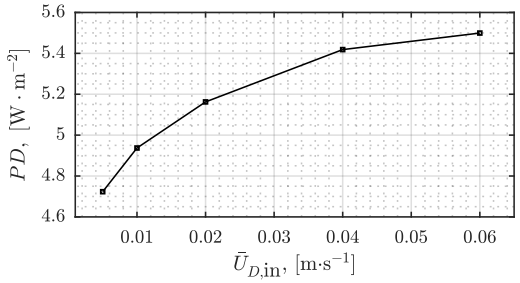

Figure 4.9: Variation in power density with varying cross flow momenta.

Figure 4.10 (a) shows stream wise concentration profiles in the draw stream in a wall normal distance of 5 μm. Towards the outlet of the channel ($x' = x/L = 1$) the lower velocities show an incomplete dilution process. It is seen that the slope $\frac{d\omega_s}{dx'}$ is strong near the inlet and rapidly approaches zero, as is attested by the central-difference gradient shown in Figure 4.10 (b). This suggests that for the lower cross flow velocities a larger fraction of the total permeation occurs towards the inlet of the draw stream.

As previously seen in Figure 4.4 (f) the permeate flux through the membrane increases exponentially at low to moderate concentrations (osmotic pressures), i.e. the lower concentration towards $x' = 1$ accommodate an exponentially decaying flux of permeate. To extract all of the Gibb's free energy the ratio of the length and height of the draw channel should approach infinity, $\frac{L}{H} \to \infty$.

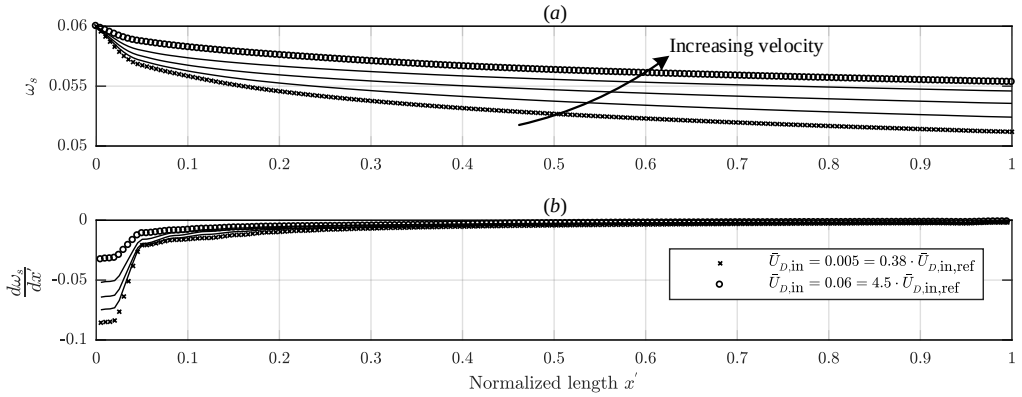

Figure 4.10: Streamwise concentration profiles (a) corresponding to varying cross flow momentum recorded along the membrane surface at $\{y, z\} = \{12.5 \cdot 10^{-3}, 2.505 \cdot 10^{-3}\}$. The stream-wise concentration gradients (b) have been evaluated as central difference derivatives.

Figure 4.11 depicts the wall normal velocity profiles along with the 50% percentile (grey area) of the integral of U_z. It is seen that the percentile is before $x' = 0.5$ and that lower inlet flow rates promote the percentile further towards the inlet. It is because of the gradient distributions in Figure 4.10 (b) that the percentile is shifted. Considering that the simulated osmotic and hydraulic pressures in the draw side are relatively low, it is expected that a draw channel with a higher L-H aspect ratio and with higher driving gradients will promote the percentile closer to the inlet. This will happen coherently as a consequence of an augmented magnitude of the $\frac{d\omega_s}{dx'}$ distribution closer to the inlet.

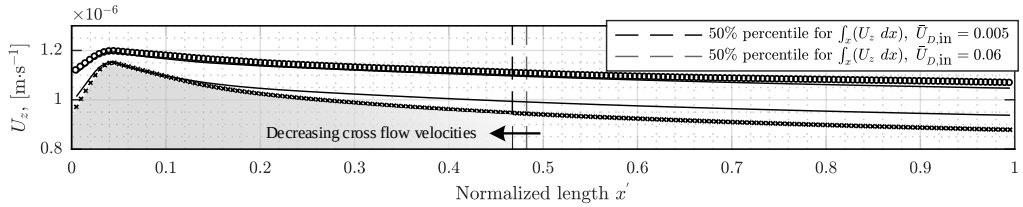

Figure 4.11: Membrane surface-normal velocities corresponding to the nomenclature in Figure 4.10.

Discussion

5

This chapter aims to discuss the findings in chapter 4 and the implemented methodology that underlies the performed simulations in this study and to identify further topics and aspects of the technology that should be addressed to make the developed model more accurate and representative.

The governing equations (3.2−3.5) all assume a laminar flow state given that turbulence modelling is not included in the framework and a steady state is assumed, i.e. the temporal derivative is zero $\frac{\rho \cdot \partial \phi}{\partial t} = 0$. Considering the Reynolds numbers for the cross flow and benchmark velocities $\{0.005, 0.0133, 0.06\}$, $Re = \{24.2, 62.8, 290\}$, in the flat sheet membrane module, and that the critical Reynolds number for laminar-to-turbulent transition for internal duct flow is $2.3 \cdot 10^3$, it is justifiable to assume the laminar state for the simulated velocities.

However, taking into account that the conventional boundary layer physics may not conform to the critical Reynolds number for the disrupted permeation boundary layer, it can be speculated that the critical number is promoted in the shear layer due to the occurrence of higher strain rates at the interface between the incoming brine phase and the permeate phase. This is conceptualized in Figure 5.1 which shows a boundary layer undergoing laminar-to-turbulent transition superpositioned with the skewed permeate velocity profile. Furthermore, in a single-phase flow only pressure diffusion occurs within the boundary layer whereas the current two-phase flow also comprises Fickian diffusion and buoyancy driven diffusion. The latter is however not simulated. This will to some extent contribute to mixing between shear layers and henceforth change the strength of their interaction. Consequently, at higher flow rates, increased vorticity incident in and around the interface may induce minor instabilities that grow until an arbitrary saturated state followed by dissipation into a fully laminar state in the downstream. It is not plausible that the instabilities will grow into the turbulent regime, but a laminar weak form of Kelvin-Helmholtz instabilities may be accommodated within the boundary layer flow.

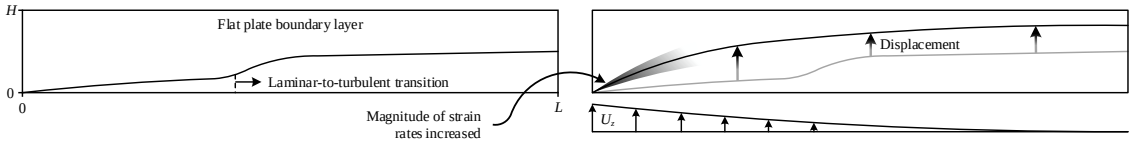

Figure 5.1: Conceptual schematics of a conventional flat plate boundary layer (left) and a boundary layer super-positioned with an assumed permeate velocity profile (right). It is assumed that the orders of magnitude of the boundary layer height and the velocity is comparable. The contours and profiles in the schematic are not drawn to scale.

To model such instabilities the source-term in the momentum equation (3.3) should model the momentum flux from the strong osmotic pressures. Assume that pure water meets the brine phase with a solute mass fraction of 6%. At the interface an unconstrained pressure difference of 48.3 bar exist that will enhance diffusion significantly.

The velocity profiles shown in Figure 4.11 suggest the presence of a deficiency in the case setup. It is not realistic for positive stream-wise velocity gradient profiles to exist as only the concentration, pressure and temperature fields at the membrane surface define these profiles. Both channels are independently isothermal and no trans-membrane heat flux occurs. I.e. the osmotic pressure is enhancing the permeation through an increasing concentration of solutes near the membrane surface where $\frac{dU_z}{dx'} > 0$ and the only possible supply for this is from the free-stream. However, this transfer requires a suction pressure that can counteract the dynamic pressure contained in the vertical permeate flow. Figure 4.10 demonstrates that the field of $\nabla_{x'}(\omega_s)$ is continuously zero or negative and the positive derivative in the U_z field can henceforth not be attributed to the concentration field.

It is suspected that the deficiency is realized from an incorrect implementation of the internal boundary in the module via the utility `createPatch`. The deficiency is only visually prominent in initialized solutions and converged solutions at very low permeation rates. It may also propagate into solutions with higher attained permeation rates. The deficiency is seen in the initialized field on the left in Figure 5.2. A possible solution to the issue is to spatially resolve only the x-z plane in 2D, excluding the third y dimension. `createPatch` may not support this. Another possible discrepancy is the implementation of the fully developed flow distribution for which its robustness is not investigated. A simple solution to produce a developed flow profile at the draw inlet is to extend the channel in the x direction as depicted in Figure 5.3. This does consequently increase computational demands with the computational domain being larger with more cells.

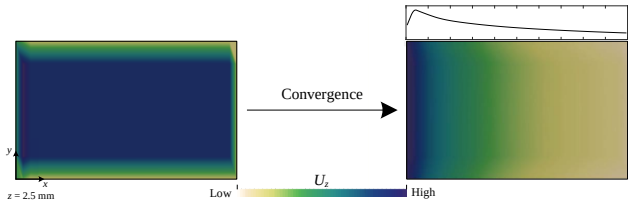

Figure 5.2: The discontinuity seen in the initialized velocity field may be retained into the converged solution.

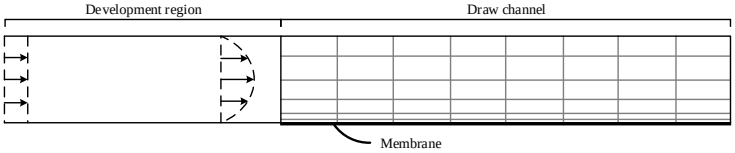

Figure 5.3: Schematic of an extended draw channel for producing a fully developed velocity profile at the draw inlet as a substitute of mapping a profile in the OF code.

The approach taken in this investigation for modelling permeation in porous media is a hybrid flow-field-resolutive/membrane-non-resolutive approach which applies a spatially non-dimensional internal boundary condition model to the assumed zero-thickness membrane. As discussed in the state of the art (section 1.3 on page 16) a very different approach to modelling the membrane process is a resolutive approach that bases the analysis of the membrane on a spatial discretization with a non-zero thickness. This methodology has both advantages and disadvantages compared to a non-resolutive approach with the major ones outlined in Table 5.1.

Table 5.1: Advantages and disadvantages of features in a resolutive versus a non-resolutive approach.

	Resolutive		*Non-resolutive*	
Feature	Advantage	Disadvantage	Advantage	Disadvantage
$^{(i)}$Modelling of transport variables	Transport equations, robust schemes.			Complex implicit formulations, schemes like Ridder's method.
Computational demand		Higher.	Lower.	
$^{(ii)}$Implementation	Well documented in OF.			Use of `topoSet`, `createBaffle` & `createPatch`.
$^{(iii)}$Customizability	Higher, additional transport variables	Computational demand.	High to a limit, complexity added via fewer equations.	$\propto$ complexity.
$^{(iv)}$Discretization	Non-uniformity in membrane, transience.	Implementation of properties through additional tensors.	No need for discretization.	Uniformity in membrane, steady-state representation.

$^{(i)}$Where the current model represents the transport of solutes and momentum through the membrane via two boundary conditions linked with the adjacent fields of $\mathbf{U}$ and ω_s a resolutive approach can use transport equations discretized spatially and temporally within the membrane to describe the transference of scalars. An example of such an equation is the saturation equation (1.25) which is implemented in the same manner as the governing equations of momentum, energy and mass continuity. However, the additional transport variables and grid cells necessitate more computational power for obtaining field solutions.

$^{(ii)}$The creation of the internal boundary connecting two spatial domains is not trivial as it involves face-mapping algorithms that link the transfer of data from the faces of the two domains that are incident at the internal boundary. Utilities such as `topoSet`, `createBaffle` and `createPatch` can be used in this regard but may prove difficult to use. Per contra, implementing additional transport equations is relatively trivial and more intuitive in comparison as it is well documented in the OF source code and tutorials.

$^{(iii)}$The current model for j_w, derived in appendix A, is complex compared to the few presented available models in section 1.3. For it to be more accurate and to be closer to being a fully

phenomenological model it ought to consider a larger parameter-space including, but not limited to:

- Porosity ε and tortuosity τ of the porous structure through the structure parameter $\mathcal{S} = \frac{t_{sl} \cdot \tau}{\varepsilon}$.
- Permeabilities $\mathcal{A}$ and $\mathcal{B}$.
- Transient phenomena leading to ICP.
- Solute resisitivity $\mathcal{R}$ for quatifying ICP.

The solute resistivity is defined by equation (5.1) where t_{sl} is the support layer thickness and $\mathcal{D}_{sw_{(m)}}$ is the solute diffusion within the porous layers [McCutcheon and Elimelech, 2006]. This parameter describes the resistance to diffusion of solute through the membrane porous layers and is consequently a measure ICP.

$$\mathcal{R} = \frac{t_{sl} \cdot \tau}{\mathcal{D}_{sw_{(m)}} \cdot \varepsilon} \tag{5.1}$$

However, it is evident that this will make the formulation of the model even more complex. The implementation of the extended parameter-space in terms of additional transport equations is simpler and does not necessarily involve the use of additional iterative numerical methods as the new transport variables are coupled to the governing equations through e.g. a SIMPLE loop.

$^{(iv)}$The main difference between the two approaches is the spatial discretization of the computational domain. In the current method the topology of the membrane is simply modelled through an effective diffusivity and thickness, but information about these is imposed through experimental values of $\mathcal{A}$ and $\mathcal{B}$ which are usually assumed constant in literature. With a discretization of the spatial domain the topology of an anisotropic membrane can be explicitly represented. Moreover, material-dependent and therefore spatially variant membrane properties can be mapped to different porous sections providing a foundation for a more detailed description of the membrane. A shortcoming of the non-resolutive approach is its inability for implementing temporal phenomena in its modelling, which for some membranes describe the accumulation of solutes inside the porous substrate. This accumulation will inevitably congest the pores and lead to ICP. There is much interest in being able to quantify and describe this accumulation considering that ICP is more degradative in comparison to ECP [McCutcheon and Elimelech, 2006]. Moreover, if the solute concentration exceeds the equilibrium solubility of the solution, scaling within the substructures of the membrane can occur [Al-Amoudi, 2010]. For a spatially discretized membrane, the transient contribution to solute transport is inferred through the temporal derivative and the accumulation of solutes in the domain can populate a sink term in the solute transport equation. However, achieving the same feature through a modelled membrane requires one or more penalization groups which mitigate the predicted j_w. Representing an accumulation in a spatially non-dimensional membrane model is more complex as there is no basis for assigning varying concentrations inside the membrane.

The simulation results show that the developed code is susceptible to machine precision errors, mainly in computations involving velocities. The length-scale of the studied geometry is 10^{-2} [m] which does not introduce floating point errors into the computations. However, considering that PRO applications in commercial perspectives utilize hollow fibre membranes that have a hydraulic diameter with an order of magnitude of $\mathcal{O}(10^{-6})$ [m] simulating with these magnitudes increases the susceptibility to floating point errors in, among other computations, the applied central difference schemes. To circumvent this eventual problem dimensional analysis can be applied. Not only can

it alleviate the sensitivity to small length scales but similarly eliminate an arbitrary number of variables in the parameter-space possibly making the model less complex.

In the prospective of inferring temperature polarization along the membrane surface via the heat transfer boundary condition which is yet to be imposed in the framework, it is important to model the thermo-physical properties as multivariant as they not only will vary with salinity but also with temperature to lesser or more significant extents. Consider for example Figures 5.4 and 5.5.

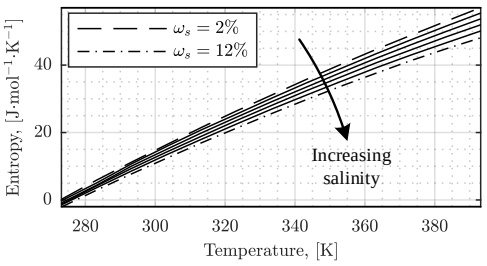

Figure 5.4: The dependence of entropy of temperature and the mass fraction of salt [Sharqawy et al., 2010].

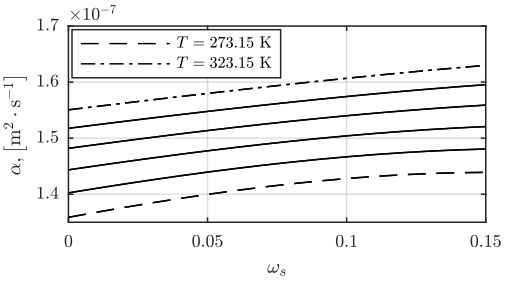

Figure 5.5: Thermal diffusivity as a function of temperature and salininty [Nayar et al., 2016].

Herein, the thermal effect on entropy and thermal diffusivity is apparent. For imposing the polarization effect in the temperature field it is essential that the thermal diffusivity is accurately modelled as it explicitly alters the spatial extent of the thermal boundary layer. Modelling of multi-variable thermo-physical properties in the OF environment is most efficiently implemented through libraries with state equations. Libraries such as CoolProp [Bell et al., 2016] may be appropriate for this. Moreover, at moderate-to-high osmotic pressures some thermophysical properties cannot be assumed linear. I.e. the relations used by Gruber et al. [2011] from data prepared by Geraldes et al. [2001] are invalid at higher osmotic pressures. Figure 5.6 show research that can attest this for at least the mixture density and viscosity. The bulk temperature will also have an effect on these properties [Nayar et al., 2016]. Polynomial fits to the data are:

$$\rho_{mix} = -407.76 \cdot \omega_s^2 + 692.63 \cdot \omega_s + 997.14 \tag{5.2}$$

$$\nu_{mix} = \left(26.6 \cdot \omega_s^2 + 6.28 \cdot \omega_s + 8.94\right) \cdot 10^{-7} \tag{5.3}$$

In relating the pressure gradient to the osmotic and temperature gradients, in equation (A.24) it is duly noted that using the ideal gas law is a simplification that induces error in to the permeation equation. Attributing a linear behaviour to the relation between the permeation rate and the Dufour effect is anomalous as the interaction between pressure forces and the elastic membrane material may be non-linear. This is preveniently suggested in Figures 1.5 and 1.6 on page 18 that by convention are coupled to the Dufour effect through $j_w = f_{\mathrm{I}}(\mathcal{A}, \Delta\pi, \Delta P, \Delta T)$ and $j_s = f_{\mathrm{II}}(\mathcal{B}, \Delta\pi, \Delta P, \Delta T)$. As has been previously stated, the pores in the membrane dilate in response to higher pressures and as a consequence an equation of state for water should be implemented, which takes into account the actual deformation response.

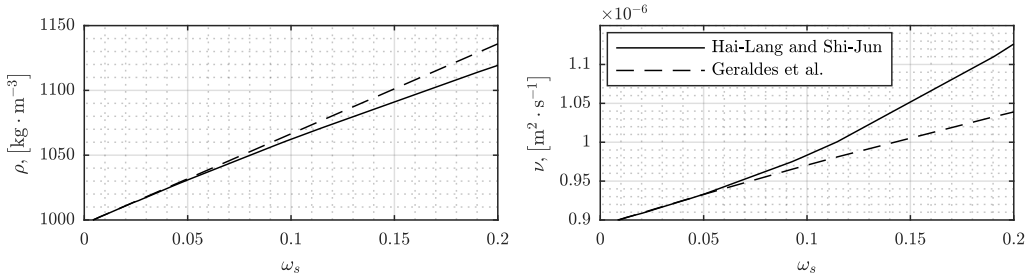

Figure 5.6: Density and kinematic viscosity as a function of mass fraction [Hai-Lang and Shi-Jun, 1996].

Figure 4.10 on page 47 shows the effect cross flow velocities has on the purging of fluid parcels of low concentration and subsequently on the permeation profile seen in Figure 4.11 where low cross flow velocities skew the permeation rate towards the inlet. The strong influence substantiates the importance of establishing a carefully chosen slip velocity through relation (1.24). This requires knowledge of the particular membrane as both the slip coefficient ζ and the permeability κ are membrane specific. From analytic theory it is known that the pressure drop through a pipe is proportional to $\bar{U}^2 \cdot \frac{L}{D_h}$. Considering the scale of a hollow fibre membrane capillary pressure may constitute a larger contribution to this pressure drop. I.e. increasing the cross-flow velocities may be beneficial until the energy-costs of compensating for the pressure drop exceed the enhancement of the permeation rate.

Finally, a more ethical question arises regarding the implementation of the technology. As is attested by Figure 4.2 (h) and various documented studies in the research community such as the investigation performed by Touati et al. [2015b] the permeation efficiency is very susceptible to the osmotic pressure at the feed side of the membrane with completely de-ionized water accommodating maximized performance. I.e. drinking water should be used as a feed which is not justifiable in regions with water-scarcity. Furthermore, the extent of these regions are currently expanding in union with anthropogenic climate changes which limits the advancement of the technology further.

Moreover, commercial membrane modules to not utilize the entire Gibb's free energy meaning that the diluted draw fluid is brackish upon exiting the module. This is evident in the data provided by Saltpower, seen in Table 5.2. Herein, the flow specifications for two modules of two diameters (5 and 10 inches, respectively) are outlined. For the 5" module it is evident that the total permeate flow rate through the membranes is equal to the inlet flow rate as $\dot{V}_{D,out} = 12 = 2 \cdot \dot{V}_{D,in}$. This means that the salt concentration at the draw outlet is half of the inlet concentration which constitutes a large fraction of free energy. This fraction can be recovered by re-injecting it into the geothermal well, but naturally the well can only support a volume equal to the extracted draw volume, so the remainder has to be discarded as wasted energy. This purged brackish solution cannot be discharged into any reservoir and is subjected to environmental regulations.

Table 5.2: In and out flow specifications for the Toyobo membrane module used by Saltpower ApS.

		Feed side		*Draw side*	
Membrane type		5"	10"	5"	10"
Flow rates L/min	In	10	30	6	40
	Out	4	12	12	58
Velocities cm/s	In	15.8	9.3	0.7	1.7
	Out	6.3	3.7	1.4	2.5

Conclusions

6

This chapter presents key results of this study and summarizes the projects findings in accordance with the problem statement in chapter 2 on page 27.

Via the state of the art analysis presented in this report a number of studies on thermal effects on membrane performance is brought forward [Traxler, 1928; Phuntsho et al., 2012; She et al., 2012; Touati et al., 2015b; Li, 2015]. The investigations emphasize that the trans-membrane permeation rate is very dependent on temperature gradients and that it is erroneous to neglect it in the modelling of membrane processes where even small temperature gradients exist. Moreover, a temperature gradient is beneficial until a certain extent after which thermally induced ICP becomes too significant. The fact that the performance is enhanced with an increasing temperature gradient can be exploited considering that extracted geothermal water often has a relatively high temperature. Optimally the PRO technology is placed inline with the geothermal water supply to a geothermal heat or combined heat and power plant. From an optimization perspective there is a symbiotic operational point where the PRO technology consumes a fraction of the heat from the geothermal water either before or after it enters the heat exchangers within the geothermal plant, so as to provide the highest membrane performance whilst still extracting a sufficient amount of heat in the heat exchangers. The relevance for considering this implementation may become more pertinent as membranes improve and attain higher performances.

Through a thorough literature review two approaches to modelling the membrane permeation process have been identified, a non-resolutive and a resolutive approach. Both aim to represent the process defined by a wide range of mechanisms and physical considerations that characterize a particular membrane. These mechanisms are defined by, among others, thermodynamics that constitute the interaction between the brine and permeate phases, polarization phenomena in temperature and concentration profiles which shift the permeation process away from the ideal reversible mixing process and parameters that describe the membrane topology. Subsequently, a non-resolutive (modelling) approach is implemented as spatial discretization of a porous medium in a resolutive approach demands more computational power. The developed membrane model is founded in a fundamental definition of a driving force from chemical potentials in concentration, hydraulic pressure and temperature and formulated in the form of a comprehensive set of implicit and explicit formulae that are solved iteratively to predict non-uniform permeation profiles along the length of a membrane.

The permeation model is coupled to the flow on either side of the membrane with the main purpose of resolving the external polarization effect in the fields of concentration and temperature. Within the time-frame of this study a boundary condition for the mass transfer across the membrane has been implemented but a boundary condition for heat transfer is yet to be completed and is

subsequently left as future work. The solutions to the flows in the channels enclosing the membrane is provided by a modified steady state and weakly compressible formulation of the semi-implicit method for pressure-linked equations (SIMPLE). During every iteration within the SIMPLE loop the permeation model is solved, in an iterative procedure with the Ridder's method for root-finding [Ridders, 1979].

It is found that permeation performance is intrinsically dependent on the physics of the boundary layer as its development alters the distribution of scalar properties incident at the membrane surface. It is these scalar distributions infinitesimally close to the surface that define the permeation strength. It has been the aim of this research to envelope an extensive range of mechanisms and properties into one comprehensive framework and conclusively a strong basis for an accurate description of the permeation performance has been procured. Nevertheless, much work still needs to go into the development and fine-tuning of the formulated model, but at this stage the model demonstrates its ability to represent the permeation rate through:

1. the non-linear dependence to the trans-membrane gradients in temperature and concentration.
2. the dependence to the flow state and momentum flux in the spatial domains encompassing the membrane.
3. the dependence on membrane properties such as thickness and membrane-in-situ solute-to-solvent diffusion $\left(\mathcal{D}_{sw_{(m)}}\right)$ which is indirectly a function of membrane porosity and tortuosity.
4. the dependence to internal and external inhibitive polarization phenomena.

In a sensitivity analysis simulations performed with the model predict that driving forces from temperature, pressure and concentration gradients all are significant and are of comparable orders of magnitude. They are primarily of a non-linear nature which is in agreement with published findings and conclusions available in literature. Concluding from this, the main message to other researchers in both academia and the industry is that in the development of membranes for PRO and more generally in the utility scale procurement of a PRO plant, it is essential to consider the governing fluid mechanics in the membrane flows in order to effectively mitigate irreversibilities in the osmotic power production and subsequently maximize the energy output of the technology. Given the examined sensitivity to the items above, it is clear that membrane performance optimization is a challenging problem.

The balance between the momenta contained in the cross-flow field and the permeate flow is determining for how much the high concentration fluid, and consequently the osmotic pressure field, is displaced from the membrane surface. Results show that higher cross-flows more effectively purge the film of low concentration fluid at the membrane surface and therefore enhance the performance. Simultaneously the membrane-perpendicular velocity profile becomes more uniformly distributed with higher velocities, whereas a large displacement of the boundary layer (low cross-flow momentum flux) leads to a more skewed profile along the membrane in the stream-wise direction. This has been examined for a saline mass fraction of $\omega_s = 6\%$, but for geothermal brines ($\omega_s > 15\%$) a uniform permeation profile is more difficult to achieve considering that the permeation mass flux is exponentially increasing with low-to-moderate osmotic pressures [0-120 bar] corresponding to $\omega_s \in [0,13.6]\%$.

Without available empirical results from analyses of particular membranes the possibility of modelling certain membrane properties is highly preferable. The prospect of including porosity and

tortuosity through either the structure parameter or the solute resistivity in an implicit model is discussed in chapter 5 and it is evident that these membrane parameters are relatively trivial to define from knowledge about the particular membrane. However, the membrane diffusivity is in this framework for the sake of simplicity assumed to be constant albeit it being a multi-dependent and variant parameter. For a model to be truly useful in commercial perspectives the dependence of $\mathcal{A}, \mathcal{B}$ and $\mathcal{D}_{sw_{(m)}}$ on e.g. internal temperature distribution, internal concentration polarization, the pressure-dependent elastic behaviour of the membrane material should be modelled. The framework herein can accommodate such a feature limited only by the fact that scalar profiles within the membrane are not resolved.

The permeation model already retains the ability to indirectly represent a dependence on the amount of solute inside the membrane through the solute concentration at the feed side of the membrane. ICP is directly correlated to this concentration as the solutes incident at the feed side membrane surface are free to percolate into the porous substructures, i.e. the model confirms that the membrane performance is extremely susceptible to the purity of the feed solution. Simulation results suggest that the energy flux is degraded by 47% in the feed solute mass fraction range of $\omega_{s,F} \in [0, 1.39]\%$ corresponding to an osmotic pressure of $\pi_{s,F} \sim [0, 11.2]$ bar. The effects of external concentration polarization on the draw side have been investigated at a moderate osmotic pressure corresponding to $\omega_{s,D} = 6\%$ and a relatively weak permeation flux. Here it is found that ECP is negligible in comparison to ICP but it is reasonable to expect the effect to be more predominant at higher osmotic pressure and higher permeation-to-cross-flow flux ratios $\left(\frac{J_w}{\dot{V}_{D,\text{in}}}\right)$ where the boundary layer growth will be less constrained by the momentum flux in the draw stream. J_w [$\text{m}^3 \cdot \text{s}^{-1}$] is the permeate flow rate and $\dot{V}_{D,\text{in}}$ is the incoming volumetric flow rate at the draw inlet.

Conclusively, this study has through the developed model and a literature review found that the contributions to the driving force from gradients in temperature and concentration are on par with pressure driven diffusion in the membrane and that they as a consequence are important to consider in PRO. The variation of all three gradients are able to enhance the permeation performance but as well significantly degrade the performance if they are too strong due to their direct connection to ICP.

Future Work

7

This chapter presents the topics and analyses the project have not addressed, which could be interesting and relevant to study further. The focus is on the immediate problems that should be addressed.

Continuing from the discussion about the boundary layer physics, future work can revolve around addressing the question concerning the premature inception of Kelvin-Helmholtz instabilities that has been posed in chapter 5. To the present authors knowledge few studies exist on the interaction between laminar jets and cross flows due to their rarity in engineering applications. It is nevertheless interesting how the transition development is altered with disruptive permeation. If the permeation profile is compared to a long extended jet that interacts with the free-stream, analogies can be drawn from studies on the interaction between laminar jets and laminar cross flow-fields such as the research performed by Brinkerhoff and Yaras [2012]. The researchers report that the shear layers roll up into Kelvin-Helmholtz-like instabilities. Their case study differs from this in the perspective that the jet Reynolds number is 6330 and the jet-to-main-flow velocity is 9.78. Nevertheless, considering that theoretically an osmotic pressure gradient $\mathcal{O}\left(10^2 \text{ bar}\right)$ can exist in the boundary layer it is interesting to investigate if the shear layers can produce roll-up vortical structures and vorticity. Per contra, numerous studies on the interaction between turbulent jets and varying crossflow-fields exist as is evident in the review by [Mahesh, 2013]. It is therein postulated that at lower velocity ratios, i.e. $\frac{U_{\text{jet}}}{U_\infty} < 1$, the shear layers in the wakes of jets are of a universally unstable nature but if this applies to very low laminar-laminar velocity ratios $\frac{U_{\text{jet}}}{U_\infty} \ll 1$ is not discussed. It is stated that higher pressure gradients in the immediate downstream of a jet can induce separation that extends to the inside of the jet, at low velocity ratios.

Perhaps implementing vortex generators in proximity to regions with the strongest transverse flow may, in combination with the promotion of the critical Reynolds number, produce sufficiently strong pressure gradients, both osmotic and hydraulic, which can accommodate laminar instabilities for an arbitrary spatial extend downstream of the jet and thereby enhance the membrane performance. The region with the stronger transverse flow is evident in Figure 4.11 on page 47 where the wall normal velocities are higher towards $x' = 0$. Further work can be invested into resolving the anticipated instabilities with the aim of investigating their time and length scales and as importantly their relation to local osmotic pressure gradients and diffusion caused by eventual temperature gradients, within the boundary layer. This may require the use of high fidelity modelling methods such as direct numerical simulation.

Regarding further development of the model the most important tasks to follow are as described in the following. One important feature to develop is the heat flux boundary condition. Its implementation will provide the discretization of a thermal boundary layer and subsequently its

polarization effects. This will also necessitate a thermo-physical model of the thermal diffusivity α. Moreover, the discrepancy described in chapter 5 should be eliminated by investigating other procedures for creating the internal boundary onto which the membrane models are imposed and the implementation of the fully developed velocity profile at the channel inlets should be analyzed for discrepancies. As concluded in chapter 6 it is preferable to make the membrane model more dependent on membrane geometrical properties such as porosity, tortuosity, thickness, etc. Lastly, a validation of the solver from external research is very important and this may ultimately require the application and adjustment of weights that scale the model exponentials defined by the three chemical potentials.

A less important but useful feature to develop can be a utility which can provide a quantification of the membrane performance through the second law efficiency so as to quantify the mitigation of irreversibilities. This can be done by evaluating the net energy flow through the membrane and the Gibb's free energy of mixing $\tilde{\Delta}G$ as the theoretically available energy in the saline fluid and from this formulate an efficiency similar to equation (7.1).

$$\eta = \frac{1}{\tilde{\Delta}G} \cdot \int PD \; dA_m \tag{7.1}$$

A farther outlook that will require an additional comprehensive investigation but an outlook that can possibly yield some interesting results is to simulate the mitigative effects on CP that centrifugal forces can induce. Pharaoh et al. [2000] report that the rotation of membranes does enhance the permeate flux due to CP mitigation.

Bibliography

Achilli et al., **2009**. Andrea Achilli, Tzahi Y. Cath and Amy E. Childress. *Power generation with pressure retarded osmosis: An experimental and theoretical investigation.* Journal of Membrane Science, 343(1-2), 42–52, 2009. doi: 10.1016/j.memsci.2009.07.006.

Al-Amoudi, **2010**. Ahmed Saleh Al-Amoudi. *Factors affecting natural organic matter (NOM) and scaling fouling in NF membranes: A review.* Desalination, 259(1-3), 1–10, 2010.

Alvarez-Silva et al., **2016**. O. A. Alvarez-Silva, A. F. Osorio and C. Winter. *Practical global salinity gradient energy potential.* Renewable and Sustainable Energy Reviews, 60, 1387–1395, 2016. doi: 10.1016/j.rser.2016.03.021.

Alvarez-Silva et al., **2014**. Oscar Alvarez-Silva, Christian Winter and Andres F. Osorio. *Salinity Gradient Energy at River Mouths.* Environmental Science and Technology Letters, 10, 410–415, 2014. doi: 10.1021/ez500239n.

Aschmoneit, **2016**. F. Aschmoneit. *A membraneFoam tutorial*, Chalmers University of Technology, 2016. URL `http://www.tfd.chalmers.se/~hani/kurser/OS_CFD_2016`.

Fynn Jerome Aschmoneit. Computational Fluid Dynamics Models of Osmotic and Electroosmotic Phenomena. PhD thesis, Technical University of Denmark, 2019.

Banat and Simandl, **1994**. Fawzi A. Banat and Jana Simandl. *Theoretical and experimental study in membrane distillation.* Desalination, 95(1), 39–52, 1994. doi: 10.1016/0011-9164(94)00005-0.

Bell et al., **2016**. Ian Bell, Jorrit Wronski, Sylvain Quoilin and Vincent Lermort. *CoolProp*, 2016. visited on 22/05/2018.

Bruno Braga. Direct Numerical Simulations of Two-Phase Flow in Porous Media: A Sensitivity Analysis of Relative Permeabilities. PhD thesis, Politecnico Milano, 2016.

Brinkerhoff and Yaras, **2012**. Joshua R. Brinkerhoff and Metin I. Yaras. *Direct Numerical Simulation of a Square Jet Ejected Transversely into an Accelerating, Laminar Main Flow.* Flow, Turbulence and Combustion, 89(4), 519–546, 2012. doi: 10.1007/s10494-012-9406-z.

Brooks and Corey, **1964**. R. H. Brooks and A. T. Corey. *Hydraulic Properties of Porous Media and Their Relation to Drainage Design.* Transactions of the ASAE, 7(1), 1964. doi: 10.13031/2013.40684.

Geankoplis, **2003**. Christie John Geankoplis. *Transport Processes and Separation Process Principles.* Prentice Hall, fourth edition edition, 2003. ISBN 978-0131013674.

Genuchten, **1980**. M. Th. Van Genuchten. *A closed-form equation for predicting the hydraulic conductivity of unsaturated soils.* Soil Science Society of America Journal, 44(5), 892–898, 1980. doi: 10.2136/sssaj1980.03615995004400050002x.

Geraldes et al., **2001**. Vítor Geraldes, Viriato Semião and Maria Norberta de Pinho. *Flow and mass transfer modelling of nanofiltration.* Journal of Membrane Science, 191(1-2), 109–128, 2001. doi: 10.1016/S0376-7388(01)00458-6.

Gruber et al., **2011**. M. F. Gruber, C. J. Johnson, C. Y. Tang, M. H. Jensen, L. Yde and C. Hélix-Nielsen. *Computational fluid dynamics simulations of flow and concentration polarization in forward osmosis membrane systems.* Journal of Membrane Science, 379, 488–495, 2011. doi: 10.1016/j.memsci.2011.06.022.

Hai-Lang and Shi-Jun, **1996**. Zhang Hai-Lang and Han Shi-Jun. *Viscosity and Density of Water + Sodium Chloride + Potassium Chloride Solutions at 298.15 K.* Journal of Chemical and Engineering Data, 41(3), 516–520, 1996. doi: 10.1021/je9501402.

Hayashi and Okumura, **2016**. Hidechito Hayashi and Tetsuya Okumura. *Macro and nano behavior of salt water in pressure retarded osmosis membrane module.* Desalination, 389, 155–161, 2016. doi: 10.1016/j.desal.2016.01.024.

Hill, **1966**. Terrell L. Hill. *Studies in Irreversible Thermodynamics.* Journal of Theoretical Biology, 10, 442–459, 1966. doi: 0022-5193(66)90137-8.

Horgue et al., **2014**. Pierre Horgue, Cyprien Soulaine, Jacques Franc, Romain Guibert and Gérald Debenest. *An open-source toolbox for multiphase flow in porous media.* Computer Physics Communications, 187, 217–226, 2014. doi: https://doi.org/10.1016/j.cpc.2014.10.005.

IEA, **November 2017**. International Energy Agency IEA. *World Energy Outlook 2017*, International Energy Agency, November 2017.

Kimura and Sourirajan, **1967**. Shoji Kimura and S. Sourirajan. *Analysis of data in reverse osmosis with porous cellulose acetate membranes used.* AIChE Journal, 13(3), 497–503, 1967. doi: doi.org/10.1002/aic.690130319.

Kuleszo et al., **2010**. Joanna Kuleszo, Carolien Kroeze, Jan Post and Balázs M. Fekete. *The potential of blue energy for reducing emissions of CO_2 and non-CO_2 greenhouse gases.* Journal of Integrative Environmental Sciences, 7, 89–96, 2010. doi: 10.1080/19438151003680850.

Lee et al., **1981**. K. L. Lee, R. W. Baker and H. K. Lonsdale. *Membranes for power generation by pressure-retarded osmosis.* Journal of Membrane Science, 8(2), 141–171, 1981. doi: 10.1016/S0376-7388(00)82088-8.

Li, **2015**. Mingheng Li. *Analysis and optimization of pressure retarded osmosis for power generation.* American Institute of Chemical Engineers, 61(4), 1233–1241, 2015. doi: 10.1002/aic.14715.

Loeb, **1976**. Sidney Loeb. *Production of energy from concentrated brines by pressure-retarded osmosis: I. Preliminary technical and economic correlations.* Journal of Membrane Science, 1, 49–63, 1976. doi: 10.1016/S0376-7388(00)82257-7.

Loeb et al., **1997**. Sidney Loeb, Leonid Titelman, Emmanuel Korngold and Joseph Freiman. *Effect of porous support fabric on osmosis through a Loeb-Sourirajan type asymmetric membrane.* Journal of Membrane Science, 129(2), 243–249, 1997. doi: 10.1016/S0376-7388(96)00354-7.

Lonsdale et al., 1965. H. K. Lonsdale, U. Merten and R. L. Riley. *Transport properties of cellulose acetate osmotic membranes.* Journal of Applied Polymer Science, 9(4), 1341–1362, 1965. doi: 10.1002/app.1965.070090413.

Mahesh, 2013. Krishnan Mahesh. *The Interaction of Jets with Crossflow.* Annual Review of Fluid Mechanics, 45, 379–407, 2013. doi: 10.1146/annurev-fluid-120710-101115.

McCutcheon and Elimelech, 2006. Jeffrey R. McCutcheon and Menachem Elimelech. *Influence of concentrative and dilutive internal concentration polarization on flux behavior in forward osmosis.* Journal of Membrane Science, 284(1-2), 237–247, 2006. doi: 10.1016/j.memsci.2006.07.049.

Miyawaki et al., 1997. Osato Miyawaki, Akiko Saito, Takeshi Matsuo and Kozo Nakamura. *Activity and Activity Coefficient of Water in Aqueous Solutions and Their Relationships with Solution Structure Parameters.* Bioscience, Biotechnology, and Biochemistry, 61(3), 466–469, 1997. doi: 10.1271/bbb.61.466.

Nayar et al., 2016. Kishor G. Nayar, Mostafa H. Sharqawy, Leonardo D. Banchik and John H.Lienhard V. *Thermophysical properties of seawater: A review and new correlations that include pressure dependence.* Desalination, 390, 1–24, 2016. doi: 10.1016/j.desal.2016.02.024.

Novaresio et al., 2011. Valerio Novaresio, María García-Camprubí, Salvador Izquierdo and Pietro Asinari. *An open-source library for the numerical modeling of mass-transfer in solid oxide fuel cells.* Computer Physics Communications, 183, 125–146, 2011. doi: 10.1016/j.cpc.2011.08.003.

Patankar and Spalding, 1972. S. V. Patankar and D. B. Spalding. *A Calculation Procedure for Heat, Mass and Momentum Transfer in Three-dimensional Parabolic Flows.* International Journal of Heat and Mass Transfer, 15, 1787, 1972.

Pharaoh et al., 2000. J. G. Pharaoh, N. Djilali and G. W. Vickers. *Fluid mechanics and mass transport in centrifugal membrane separation.* Journal of Membrane Science, 176, 277–289, 2000. doi: 10.1016/s0376-7388(00)00457-9.

Phattaranawik and Jiraratananon, 2001. Jirachote Phattaranawik and Ratana Jiraratananon. *Direct contact membrane distillation: effect of mass transfer on heat transfer.* Journal of Membrane Science, 188(1), 137–143, 2001. doi: 10.1016/S0376-7388(01)00361-1.

Phuntsho et al., 2012. Sherub Phuntsho, Saravanamuthu Vigneswaran, Jaya Kandasamy, Seungkwan Hong, Sangyoup Lee and Ho Kyong Shon. *Influence of temperature and temperature difference in the performance of forward osmosis desalination process.* Journal of Membrane Science, 415-416, 734–744, 2012. doi: 10.1016/j.memsci.2012.05.065.

Raeini et al., 2014. Ali Q. Raeini, Martin J. Blunt and Branko Bijeljic. *Direct simulations of two-phase flow on micro-CT images of porous media and upscaling of pore-scale forces.* Advances in Water Resources, 74, 116–126, 2014. doi: 10.1016/j.advwatres.2014.08.012.

Rahman and Saghir, 2014. M. A. Rahman and M. Z. Saghir. *Thermodiffusion or Soret effect: Historical review.* International Journal of Heat and Mass Transfer, 73, 693–705, 2014. doi: 10.1016/j.ijheatmasstransfer.2014.02.057.

Ramon et al., **2011**. Guy Z. Ramon, Benjamin J. Feinberg and Eric M. V. Hoek. *Membrane-based production of salinity-gradient power.* Energy and Environmental Science, 4, 4423–4434, 2011. doi: 10.1039/C1EE01913A.

Ridders, **1979**. C. Ridders. *A new algorithm for computing a single root of a real continuous function.* IEEE Transactions on Circuits and Systems, 26(11), 979–98, 1979. doi: 10.1109/TCS.1979.1084580.

Sharqawy et al., **2010**. Mostafa H. Sharqawy, John H. Lienhard and Syed M. Zubair. *Thermophysical properties of seawater: a review of existing correlations and data.* Desalination and Water Treatment, 16, 354–380, 2010. doi: 10.5004/dwt.2010.1079.

She et al., **2012**. Qianhong She, Xue Jin and Chuyang Y. Tang. *Osmotic power production from salinity gradient resource by pressure retarded osmosis: Effects of operating conditions and reverse solute diffusion.* Journal of Membrane Science, 401-402, 262–273, 2012. doi: 10.1016/j.memsci.2012.02.014.

Tiraferri et al., **2013**. A. Tiraferri, Y. Y. Ngai, A. Straub, S. RV. Castrillon and M. Elimelech. *A method for the simultaneous determination of transport and structural parameters of forward osmosis membranes.* Journal of Membrane Science, 444, 523–538, 2013. doi: 10.1016/j.memsci.2013.05.023.

Touati et al., **2015a**. Khaled Touati, Alberto de la Calle, Fernando Tadeo, Lidia Roca, Thomas Schiestel and Diego-César Alarcón-Padilla. *Energy recovery using salinity differences in a multi-effect distillation system.* Desalination and Water Treatment, 55(11), 3048–3055, 2015. doi: 10.1080/19443994.2014.940648.

Touati et al., **2015b**. Khaled Touati, Christoper Hänel, Fernando Tadeo and Thomas Schiestel. *Effect of the feed and draw solution temperatures on PRO performance: Theoretical and experimental study.* Desalination, 365, 182–195, 2015. doi: 10.1016/j.desal.2015.02.016.

Touati et al., **2017**. Khaled Touati, Fernando Tadeo, Sung Hoe Chae, Joon Ha Kim and Oscar Alvarez-Silva. *Pressure Retarded Osmosis: Renewable Energy Generation and Recovery.* Elsevier Science Publishing Co. Inc., 2017. ISBN 978-0-12-812103-0. doi: 10.1016/B978-0-12-812103-0.00001-5.

Traxler, **1928**. R. N. Traxler. *The Effect of Temperature on Rate of Osmosis.* Journal of Physical Chemistry, 32(1), 127–141, 1928. doi: 10.1021/j150283a010.

Wang et al., **2016**. Yang Wang, Wei He and Hai Zhu. *Computational fluid dynamics (CFD) based modelling of osmotic energy generation using pressure retarded osmosis (PRO).* Desalination, 389, 98–107, 2016. doi: 10.1016/j.desal.2016.02.002.

Wardeh and Morvan, **2008**. S. Wardeh and H. Morvan. *CFD simulations of flow and concentration polarization in spacer-filled channels for application to water desalination.* Chemical Engineering Research and Design, 86(10A), 1107–1116, 2008. doi: 10.1016/j.cherd.2008.04.010.

Wijmans and Baker, **1995**. J. G. Wijmans and R. W. Baker. *The solution-diffusion model: a review.* Journal of Membrane Science, 107, 1–21, 1995. doi: 10.1016/0376-7388(95)00102-I.

Wiley and Fletcher, **2002**. Dianne. E. Wiley and David F. Fletcher. *Computational fluid dynamics modelling of flow and permeation for pressure-driven membrane processes.* Desalination, 145(1-3), 183–186, 2002. doi: 10.1016/S0011-9164(02)00406-X.

Wiley and Fletcher, **2003**. Dianne. E. Wiley and David F. Fletcher. *Techniques for computational fluid dynamics modelling of flow in membrane channels.* Journal of Membrane Science, 211(1), 127–137, 2003. doi: 10.1016/S0376-7388(02)00412-X.

Xu et al., **2009**. Yuan Xu, Xiaoyu Peng, Chuyang Y. Tang, Q. Shiang Fu and Shengzhe Nie. *Effect of draw solution concentration and operating conditions on forward osmosis and pressure retarded osmosis performance in a spiral wound module.* Journal of Membrane Science, 348(1-2), 298–309, 2009. doi: 10.1016/j.memsci.2009.11.013.

Yip et al., **2011**. Ngai Yin Yip, Alberto Tiraferri, William A. Phillip, Jessica D. Schiffman, Laura A. Hoover, Yu Chang Kim and Menachem Elimelech. *Thin-Film Composite Pressure Retarded Osmosis Membranes for Sustainable Power Generation from Salinity Gradients.* Environmental Science and Technology, 45(10), 4360–4369, 2011. doi: 10.1021/es104325z.

Zhao et al., **2005**. Yu Zhao, James S. Taylor and Shankar Chellam. *Predicting RO/NF water quality by modified solution diffusion model and artificial neural networks.* Journal of Membrane Science, 263, 38–46, 2005. doi: 10.1016/j.memsci.2005.04.004.

Çengel and Boles, **2011**. Yunus A. Çengel and Michael A. Boles. *Thermodynamics: An Engineering Approach.* McGraw Hill, 7. edition, 2011. ISBN 978-0-07-352932-5.

Appendix: Formulation of the implicit permeation model

A

This appendix aims to show the basis for the conventional relation used to link thermodynamic driving forces from gradients in osmotic pressure, hydraulic pressure and temperature to the permeation flux through a porous medium, $j_w = f(\Delta\pi, \Delta P, \Delta T)$. The physics behind it is the core concept of the membrane processes.

A.1 Derivation of the water and salt permeability equations

Lonsdale et al. [1965] proposed the original solution-diffusion model for cellulose acetate osmotic membranes, that have been applied to common osmotic processes, such as dialysis and reverse osmosis. The widely applied relation for describing the permeation through porous media, equation (A.1) is derived through the solution-diffusion model to account for pressure gradients, and concentration gradients as the main driving forces for the permeation. In the following, the derivation of the formula, will be presented to give a basis for understanding the main drivers in osmotic processes. The following derivation is adopted from Wijmans and Baker [1995].

$$j_w = \mathcal{A} \cdot (\Delta\pi - \Delta P) \tag{A.1}$$

The mathematical formulation of the permeation in porous materials is developed from the thermodynamic principle, that the permeation is defined by the interrelated driving forces of concentration, temperature, pressure, and not relevant to this project, electromotive force. The flux of water species w or other relevant solvents across a porous medium, is proportional to the gradient in chemical potential cf. equation (A.2).

$$j_w = -L_w \cdot \frac{dM_w}{dx} \tag{A.2}$$

In the relation, L_w is a proportionality constant and ∇M_w is the chemical potential gradient, across a porous medium. This formulation links all of the driving forces, through the chemical potential, to the permeation flux. For liquids the chemical potential is defined as relation (A.3).

$$dM_w = R\bar{T}\ d\ln(\gamma_w \chi_w) + v_w\ dp \quad \rightarrow \quad M_w = M_w^0 + R\bar{T} \cdot \ln(\gamma_w \chi_w) + v_w \left(P - P_w^0\right) \tag{A.3}$$

Here, superscript 0 denotes a pure phase w, at a reference pressure P_w^0. R is the gas constant and $\bar{T}$ is the bulk temperature of the two states. γ_w is an activity coefficient for component w and χ_w is the mole fraction of the same species, in a binary or ternary mixture. $\gamma_w \chi_w$ is the activity of species w. v_w is the phase specific molar volume. By convention, the reference pressure is taken as the saturation pressure of component w, so that $P_w^0 = P_w^{\text{sat}}$. The variation in the activity coefficient of water is depicted in Figure A.1.

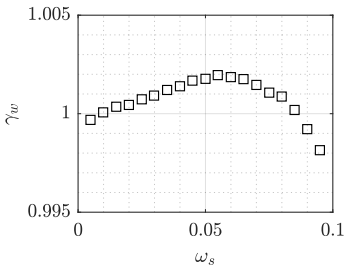

Figure A.1: Dependence of the water activity coefficient on the concentration of salt in a one-component sodium chloride aqueous mixture computed by Miyawaki et al. [1997].

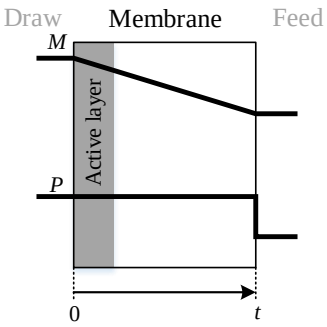

Figure A.2: Nomenclature in a cross section of a membrane.

The activity coefficient γ_w accounts for the deviations in a real mixture, from an ideal behaviour in the interaction between components. Expressing properties in terms of concentration assumes that the interaction between any pair of species in the mixture is uniform. Considering the scale of the coefficient values a water-NaCl solution is close to ideal. At this point, the following assumptions have been made:

i. In the chemical potential, thermodynamic irreversibilities are not included. A procedure for including these can be adopted from Hill [1966].
ii. Relation (A.3) only includes effects from the driving forces of pressure and concentration, i.e. the driving force of temperature is not included.
iii. The use of the gas constant in equation (A.3) for incompressible fluids and the membrane phase, is assumed to introduce negligible error.

There are two models for formulating the permeation flux, that differ in how the driving forces are included in the chemical potential. The solution-diffusion model assumes that the pressure throughout the membrane is constant and that ∇M_w is described only by a concentration gradient. The pore-flow model assumes the concentration throughout the membrane to be constant, and ∇M_w to be expressed only by a pressure gradient. In the solution-diffusion model, the differential in chemical potential in equation (A.2) is substituted by relation (A.3) where $\cancelto{0}{v_w\, dp}$. A similar approach is adopted for the pore-flow model, just where $\cancelto{0}{R\bar{T}\, d\ln(\gamma_w \chi_w)}$. When the substitutions and simplifications are done, a relation similar to Fick's law (equation (A.4)), and Darcy's law (equation (A.5)) are obtainable.

$$j_w = -\frac{R\bar{T}L_w}{\chi_w} \cdot \frac{d\chi_w}{dx} \qquad \text{(A.4)} \qquad j_w = \frac{k(P_0 - P_t)}{t} \qquad \text{(A.5)}$$

Here, $\frac{R\bar{T}L_w}{\chi_w}$ is replaced by a diffusion coefficient, $\mathcal{D}_w$, k is $L_w \cdot v_w$, and P_0 and P_t are the pressures at the interfaces between the membrane surface and the draw and feed stream, respectively. Relation (A.4) is integrated over the membrane thickness t, to yield equation (A.6).

$$j_w = \frac{\mathcal{D}_w \left(\chi_{w,0_{(m)}} - \chi_{w,t_{(m)}}\right)}{t} \qquad \text{(A.6)}$$

In this, $\chi_{w,0_{(m)}}$ and $\chi_{w,t_{(m)}}$ are the concentrations of the w phase at the previously mentioned interfaces, but inside the membrane medium. This flux can be rewritten into $j_w = \mathcal{A}(\Delta\pi - \Delta P)$ through a series of assumptions. Under the assumption that the chemical potential profile is continuous through the membrane and henceforth that the potentials at either side of the interface

at the draw side are equal, the following equality (A.7) applies.

$$
\begin{gathered}
M_{w,0} = M_{w,0_{(m)}} \\
\downarrow \\
\cancel{M_w^0} + R\bar{T}\ln\left(\gamma_{w,0}\chi_{w,0}\right) + \cancel{v_w(P_0 - P_w^{sat})} = \cancel{M_w^0} + R\bar{T}\ln\left(\gamma_{w,0_{(m)}}\chi_{w,0_{(m)}}\right) + \cancel{v_{w_{(m)}}(P_0 - P_w^{sat})} \\
\downarrow \\
\cancel{R\bar{T}}\ln\left(\gamma_{w,0}\chi_{w,0}\right) = \cancel{R\bar{T}}\ln\left(\gamma_{w,0_{(m)}}\chi_{w,0_{(m)}}\right) \\
\downarrow \\
\chi_{w,0_{(m)}} = \frac{\gamma_{w,0}}{\gamma_{w,0_{(m)}}} \cdot \chi_{w,0}
\end{gathered}
\tag{A.7}
$$

Here, the ratio of activity coefficients, is called the sorption coefficient, $K_w = \frac{\gamma_{w,0}}{\gamma_{w,0_{(m)}}}$. In the procedure above it is assumed that the molar volume at either side of the interface in the draw side, is equal. Following the same procedure on the feed side of the membrane, with equalizing the chemical potentials from equation (A.3), yields equation (A.8).

$$
\begin{gathered}
\cancel{M_w^0} + R\bar{T}\ln\left(\gamma_{w,t}\chi_{w,t}\right) + v_w(P_t - P_w^{sat}) = \cancel{M_w^0} + R\bar{T}\ln\left(\gamma_{w,t_{(m)}}\chi_{w,t_{(m)}}\right) + v_w(P_0 - P_w^{sat}) \\
\downarrow \\
\ln\left(\gamma_{w,t}\chi_{w,t}\right) = \ln\left(\gamma_{w,t_{(m)}}\chi_{w,t_{(m)}}\right) + \frac{v_w(P_0 - P_t)}{R\bar{T}}
\end{gathered}
\tag{A.8}
$$

Rearranging equation (A.8) and reformulating for the sorption coefficient, yields equation (A.9).

$$
\chi_{w,t_{(m)}} = K_w \cdot \chi_{w,t} \cdot \exp\left(\frac{-v_w\left(P_0 - P_t\right)}{R\bar{T}}\right) \tag{A.9}
$$

Substituting equations (A.7) and (A.9) into the integrated Fick's law, equation (A.6) yields equation

$$
j_w = \frac{\mathcal{D}_w K_w}{t} \cdot \left[\chi_{w,0} - \chi_{w,t}\ \exp\left(\frac{-v_w\left(P_0 - P_t\right)}{R\bar{T}}\right)\right] \tag{A.10}
$$

Further simplification can be made knowing that at osmotic equilibrium ($\Delta\pi = \Delta P$), the transmembrane permeation flux is zero, $j_w = 0$, i.e. equation (A.11) applies.

$$
j_w = 0 = \frac{\mathcal{D}_w K_w}{t} \cdot \left[\chi_{w,0} - \chi_{w,t}\ \exp\left(\frac{-v_w\Delta\pi}{R\bar{T}}\right)\right] \quad \rightarrow \quad \chi_{w,t} = \chi_{w,0}\ \exp\left(\frac{v_w\Delta\pi}{R\bar{T}}\right) \tag{A.11}
$$

This result can be combined with equation (A.10) to yield equation (A.12).

$$
j_w = \frac{\mathcal{D}_w K_w \chi_{w,0}}{t}\left[1 - \exp\left(\frac{-v_w\left(\Delta P - \Delta\pi\right)}{R\bar{T}}\right)\right] \tag{A.12}
$$

Knowing that $1 - \exp x \rightarrow x$ as $x \rightarrow 0$, this results reduces to equation (A.13).

$$
j_w = \frac{\mathcal{D}_w \cdot K_w \cdot \chi_{w,0} \cdot v_w \cdot (\Delta P - \Delta\pi)}{t \cdot R\bar{T}} = \mathcal{A} \cdot (\Delta P - \Delta\pi), \quad \mathcal{A} = \frac{\mathcal{D}_w \cdot K_w \cdot \chi_{w,0} \cdot v_w}{t \cdot R \cdot T} \tag{A.13}
$$

Similarly for the s phase, which represents the solute, a reverse salt flux can be approximated by (A.14).

$$j_s = \frac{\mathcal{D}_s K_s}{t}\left[\chi_{s,0} - \chi_{s,t}\,\cancel{\exp\left(\frac{-v_s\cdot\Delta P}{R\bar{T}}\right)}\right]^{1} \tag{A.14}$$

The exponential term approaches 1, as $\frac{-v_s\cdot\Delta P}{R\bar{T}} \to 0$. Thus, the reverse salt flux can be written as per equation (A.15).

$$j_s = \mathcal{B}\cdot(\chi_{s,0} - \chi_{s,t}), \quad \mathcal{B} = \frac{\mathcal{D}_s K_s}{t} \tag{A.15}$$

At higher differential pressures the limits of the exponential terms, $\left[\cancel{\exp\left(\frac{-v_s\cdot\Delta P}{R\bar{T}}\right)}\right]^{1}$ and $\left[1-\cancel{\exp\left(\frac{-v_w(\Delta P-\Delta\pi)}{R\bar{T}}\right)}\right]^{-v_w(\Delta P-\Delta\pi)/R\bar{T}}$, do introduce an error, the latter to a negligible extent. At $\Delta P = 100$ bar and $\bar{T} = 293.15$ K the error for the former term is 7%.

A.2 Derivation of the water and salt permeability equations, with temperature dependence

Formulating a temperature dependent framework starts with considering the contribution to the chemical potential, from a temperature difference, $\Delta T = T_t - T_0$. Here the corresponding chemical potential is $s_w \cdot dT$ so that the full potential is written as:

$$dM_w = R\bar{T}\; d\ln(\gamma_w\chi_w) + v_w dP - s_w\; dT \tag{A.16}$$

This relation has to be integrated. Integrating $s_w\; dT$ cannot be done assuming s_w constant as it is strongly variant with temperature as seen in Figure 5.4. A linear interpolation of an intermediate salinity of $\omega_s = 8\%$ is employed and its integration from a reference saturation state to the current state of w yields:

$$\begin{aligned}\int_{\text{sat}} s_w\; dT &= \int_{\text{sat}} 0.4859\cdot T - 133.48\; dT = \frac{0.4859}{2}\left(T_w^2 - T_w^{\text{sat}^2}\right) - 133.48\cdot\left(T_w - T_w^{\text{sat}}\right)\\ &= S_w^{\int_{\text{sat}} dT}\end{aligned} \tag{A.17}$$

The integration of the remaining terms yields:

$$M_w = M_w^0 + R\bar{T}\cdot\ln(\gamma_w\chi_w) + v_w\left(P_w - P_w^{\text{sat}}\right) - S_w^{\int dT} \tag{A.18}$$

Similarly as in section A.1, the equation above is balanced over the interface between the fluid continuum, subscript 0, and the membrane surface, denoted subscript $_{(m)}$:

$$M_{w,0} = M_{w,0_{(m)}}$$
$$\downarrow$$

$$\cancel{M_w^{\text{sat}}} + R\bar{T}\ln\left(\gamma_{w,0}\chi_{w,0}\right) - \left[\frac{0.4859}{2}\left(T_t^2 - \cancel{T_w^{\text{sat}^2}}\right) - 133.48\left(T_t - \cancel{T_w^{\text{sat}}}\right)\right] + \cancel{v_w\left(P_0 - P_w^{\text{sat}}\right)} =$$

$$\left.\cancel{M_w^{\text{sat}}} + R\bar{T}\ln\left(\gamma_{w,0}\chi_{w,0}\right) - \left[\frac{0.4859}{2}\left(T_0^2 - \cancel{T_w^{\text{sat}^2}}\right) - 133.48\left(T_0 - \cancel{T_w^{\text{sat}}}\right)\right] + \cancel{v_w\left(P_0 - P_w^{\text{sat}}\right)}\right|_{(m)} \tag{A.19}$$

Herein, it is assumed that $v_w = v_{w_{(m)}}$. It is assumed that the active layer is a perfect thermal barrier to the draw stream, so that a discontinuous temperature profile, as in Figure A.3, applies. The equation above can be rearranged to yield $\chi_{w,0_{(m)}}$:

$$\chi_{w,0_{(m)}} = \chi_{w,0}\cdot\frac{\gamma_{w,0}}{\gamma_{w,0_{(m)}}} - \overbrace{\exp\left(\frac{S_w^{\int_t dT}}{\bar{T}R}\right)}^{e_{\Delta T}}\gamma_{w,0_{(m)}}^{-1} \tag{A.20}$$

where,

$$S_w^{\int_t dT} = \frac{0.4859}{2}\left(T_t^2 - T_0^2\right) - 133.48\left(T_t - T_0\right) \tag{A.21}$$

Similarly on the feed side, the same concentration relation remains, as in equation (A.9). So,

$$\chi_{w,t_{(m)}} = K_w\cdot\chi_{w,t}\cdot\overbrace{\exp\left(\frac{-v_w\cdot\Delta P}{R\bar{T}}\right)}^{e_{\Delta P}} \tag{A.22}$$

Substituting these into the integrated Fick's law, yields:

$$\begin{aligned} j_w &= \frac{\mathcal{D}_w\cdot\left(\chi_{w,0_{(m)}} - \chi_{w,t_{(m)}}\right)}{t} = \frac{D_w}{t}\cdot\left[\chi_{w,0}\cdot K_w - e_{\Delta T}\cdot\gamma_{w,0_{(m)}}^{-1} - K_w\chi_{w,t}\cdot e_{\Delta P}\right] \\ &= \frac{D_w K_w}{t}\cdot\left[\chi_{w,0} - e_{\Delta T}\cancel{\gamma_{w,0}} - \overbrace{\frac{1}{\gamma_{w,0_{(m)}}\cdot K_w}\chi_{w,t}}\cdot e_{\Delta P}\right] \end{aligned} \tag{A.23}$$

At osmotic equilibrium, i.e. $j_w = 0$, the exerted hydraulic pressure is $\Delta P = \Delta\pi + \Delta T\cdot {}^{R}/_{v_w}$, assuming that the ideal gas law applies.

$$j_w = 0 = \left[\chi_{w,0} - e_{\Delta T}\gamma_{w,0} - \chi_{w,t}\cdot\overbrace{\exp\left(\frac{-v_w\cdot\left(\Delta\pi + \Delta T\frac{R}{v_w}\right)}{R\bar{T}}\right)}^{-e_{\Delta\pi\Delta T}}\right] \tag{A.24}$$

The solution to this is,

$$\chi_{w,t} = \exp\left(v_w\frac{\Delta\pi + \Delta T\frac{R}{v_w}}{R\bar{T}}\right)\cdot\left[\chi_{w,0} - e_{\Delta T}\cdot\gamma_{w,0}\right] \tag{A.25}$$

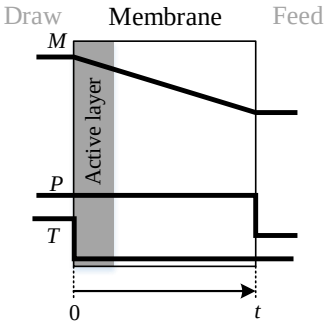

Figure A.3: Assumed profiles of the chemical potential, pressure and temperature.

This results combined with equation (A.23) yields,

$$j_w = \frac{D_w \cdot K_w}{t} \cdot [\chi_{w,0} - e_{\Delta T} \cdot \gamma_{w,0} - e_{\Delta\pi\Delta T} \cdot (\chi_{w,0} - e_{\Delta T} \cdot \gamma_{w,0}) \cdot e_{\Delta P}] \tag{A.26}$$

To simplify the use of this relation, it can be rewritten to include the permeability coefficient $\mathcal{A}$ as in section A.1. Then the final expression is:

$$j_w = \mathcal{A} \cdot \left(\left[R\bar{T} \left\{ \chi_{w,0} - \gamma_{w,0} \cdot e_{\Delta T} - e_{\Delta\pi,\Delta T} \cdot e_{\Delta P} \left(\chi_{w,0} - \gamma_{w,0} \cdot e_{\Delta T} \right) \right\} \right] \cdot \frac{1}{\chi_{w,0} \cdot v_w} \right) \tag{A.27}$$

where the dimensionless exponential terms are as follows:

$$e_{\Delta T} = \exp\left(\frac{S_w^{\int_t dT}}{R\bar{T}} \right) \tag{A.28}$$

$$e_{\Delta P} = \exp\left(-\frac{\Delta P \cdot v_w}{R\bar{T}} \right) \tag{A.29}$$

$$e_{\Delta\pi,\Delta T} = \exp\left(v_w \frac{\Delta\pi + \Delta T \cdot R \cdot v_w^{-1}}{R\bar{T}} \right) \tag{A.30}$$

Similarly, a temperature dependent relation for the solute phase can be formulated. For this phase equation (A.23) also applies and can accordingly be rewritten to:

$$j_s = \frac{\mathcal{D}_s K_s}{t} \cdot (\chi_{s,0} - e_{\Delta T}\gamma_{s,0} - \chi_{s,t} \cdot e_{\Delta P}) = \mathcal{B} \cdot (\chi_{s,0} - e_{\Delta T}\gamma_{s,0} - \chi_{s,t} \cdot e_{\Delta P}) \tag{A.31}$$

I.e. the flux equation is:

$$j_s = \frac{\mathcal{D}_s K_s}{t} \cdot (\chi_{s,0} - e_{\Delta T}\gamma_{s,0} - \chi_{s,t} \cdot e_{\Delta P}) \tag{A.32}$$

A.3 Derivation of the implicit permeation equation with reverse solute flux

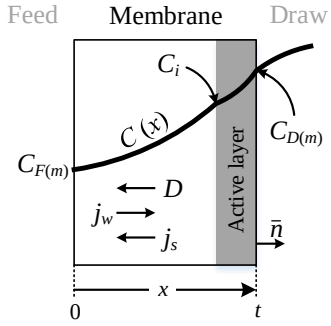

Figure A.4: Nomenclature of the concentration profile through a membrane. It is noted that size of the active layer is exaggerated.

To form an implicit correlation for j_w requires combining equations (A.27) and (A.32). The procedure for obtaining the implicit correlation with temperature dependence is presented in the following. Formulating vectorized diffusion as,

$$\bar{D} = -\mathcal{D}_{\text{eff}} \cdot \frac{d}{dx \cdot \bar{n}} \tag{A.33}$$

can be used in a solute balance $\bar{j}_s = \chi \cdot \bar{j}_w - \bar{D}$, to yield:

$$j_s = \mathcal{D}_{\text{eff}} \cdot \frac{d}{dx}\chi - j_w \cdot \chi \tag{A.34}$$

The nomenclature shown in Figure A.4 applies and will also be used going forward. The concentration profile can be modelled with an exponential cf. the equation below:

$$\chi(x) = a \cdot \exp\left(\frac{j_w}{\mathcal{D}_{\text{eff}}}x\right) + b \tag{A.35}$$

Combining this result with equation (A.34) yields,

$$\begin{aligned} j_s &= \mathcal{D}_{\text{eff}}\frac{d}{dx}\left[a\exp\left(\frac{j_w}{\mathcal{D}_{\text{eff}}}x\right)+b\right] - j_w \cdot \left[a\exp\left(\frac{j_w}{\mathcal{D}_{\text{eff}}}x\right)+b\right] \\ &= \cancel{\mathcal{D}_{\text{eff}}} \cdot \frac{j_w}{\cancel{\mathcal{D}_{\text{eff}}}} \cdot \left[a\exp\left(\frac{j_w}{\mathcal{D}_{\text{eff}}}x\right)\right] - j_w \cdot \left[a\exp\left(\frac{j_w}{\mathcal{D}_{\text{eff}}}x\right)+b\right] \\ &= \cancel{j_w \cdot a \cdot \exp\left(\frac{j_w}{\mathcal{D}_{\text{eff}}}x\right)} - \cancel{j_w \cdot a \cdot \exp\left(\frac{j_w}{\mathcal{D}_{\text{eff}}}x\right)} - j_w \cdot b \\ \therefore \quad b &= \frac{-j_s}{j_w} \end{aligned} \tag{A.36}$$

To formulate a, $\chi(x)$ at $x = 0$ is evaluated, where $\chi(x) = \chi_{F_{(m)}}$:

$$\chi(0) = a \cdot \exp\left(\frac{j_w}{\mathcal{D}_{\text{eff}}} \cdot 0\right) - \frac{j_s}{j_w} = a - \frac{j_s}{j_w} \quad \leftrightarrow \quad a = \chi_{F_{(m)}} + \frac{j_s}{j_w} \tag{A.37}$$

Thus,

$$\chi(x) = \left[\chi_{F_{(m)}} + \frac{j_s}{j_w}\right] \cdot \exp\left(\frac{j_w}{\mathcal{D}_{\text{eff}}}x\right) - \frac{j_s}{j_w} \tag{A.38}$$

Evaluating the result at $x = t_{\text{eff}}$ can be used to formulate χ_i:

$$\chi_i = \chi(t_{\text{eff}}) = \left[\chi_{F_{(m)}} + \frac{j_s}{j_w}\right] \cdot \overbrace{\exp\left(j_w \cdot \mathcal{K}\right)}^{e_{\mathcal{K}}} - \frac{j_s}{j_w} \tag{A.39}$$

where $\mathcal{K} = \frac{t_{\text{eff}}}{\mathcal{D}_{\text{eff}}}$. Combining this result with equation (A.32) yields,

$$\chi_i = \left[\chi_{F_{(m)}} + \frac{\mathcal{B} \cdot \left(\chi_{D_{(m)}} - \chi_i - e_{\Delta T}\gamma_i\right)}{j_w}\right] \cdot e_{\mathcal{K}} - \frac{\mathcal{B} \cdot \left(\chi_{D_{(m)}} - \chi_i - e_{\Delta T}\gamma_i\right)}{j_w} \tag{A.40}$$

where the reverse salt flux is defined from the concentrations across the active layer and the sign of j_s is changed due to the reversal of the x-axis. This result can be partitioned into,

$$\chi_i = \chi_{F_{(m)}} \cdot e_{\mathcal{K}} + \frac{\mathcal{B} \cdot \left(\chi_{D_{(m)}} - \chi_i - e_{\Delta T}\gamma_i\right)}{j_w} e_{\mathcal{K}} - \frac{\mathcal{B} \cdot \chi_{D_{(m)}}}{j_w} + \frac{\mathcal{B} \cdot \chi_i}{j_w} - \frac{\mathcal{B} \cdot e_{\Delta T} \cdot \gamma_i}{j_w}$$

$$= \chi_{F_{(m)}} \cdot e_{\mathcal{K}} + \chi_{D_{(m)}} \cdot \frac{\mathcal{B}}{j_w} \cdot (e_{\mathcal{K}} - 1) - \chi_i \cdot \frac{\mathcal{B}}{j_w} \cdot (e_{\mathcal{K}} - 1) + e_{\Delta T} \cdot \gamma_i \cdot \frac{\mathcal{B}}{j_w}(e_{\mathcal{K}} - 1)$$

$$\updownarrow$$

$$\chi_i \left[1 + \frac{\mathcal{B}}{j_w} \cdot (e_{\mathcal{K}} - 1)\right] = \chi_{F_{(m)}} \cdot e_{\mathcal{K}} + \chi_{D_{(m)}} \cdot \frac{\mathcal{B}}{j_w} \cdot (e_{\mathcal{K}} - 1) + e_{\Delta T} \cdot \gamma_i \cdot \frac{\mathcal{B}}{j_w}(e_{\mathcal{K}} - 1)$$

$$\updownarrow$$

$$\chi_i = \frac{j_w \cdot \chi_{F_{(m)}} \cdot e_{\mathcal{K}} + \chi_{D_{(m)}} \cdot \mathcal{B} \cdot (e_{\mathcal{K}} - 1) + e_{\Delta T} \cdot \gamma_i \cdot \mathcal{B}(e_{\mathcal{K}} - 1)}{j_w + \mathcal{B} \cdot (e_{\mathcal{K}} - 1)} \tag{A.41}$$

This can be used in the formulation of the osmotic efficiency,

$$\frac{\Delta\pi_{\text{eff}}}{\Delta\pi} = \frac{\chi_{D_{(m)}} - \chi_i}{\chi_{D_{(m)}} - \chi_{F_{(m)}}} = \frac{1}{1 - \frac{\chi_{F_{(m)}}}{\chi_{D_{(m)}}}} \cdot \left(1 - \frac{\chi_i}{\chi_{D_{(m)}}}\right) \tag{A.42}$$

Combining this result with equation (A.41) yields,

$$= \frac{1}{1 - \frac{\chi_{F_{(m)}}}{\chi_{D_{(m)}}}} \cdot \left\{1 - \frac{1}{\chi_{D_{(m)}}} \left[\frac{j_w \cdot \chi_{F_{(m)}} \cdot e_{\mathcal{K}} + \chi_{D_{(m)}} \cdot \mathcal{B} \cdot (e_{\mathcal{K}} - 1) + e_{\Delta T} \cdot \gamma_i \cdot \mathcal{B}(e_{\mathcal{K}} - 1)}{j_w + \mathcal{B} \cdot (e_{\mathcal{K}} - 1)}\right]\right\}$$

$$= \frac{1}{1 - \frac{\chi_{F_{(m)}}}{\chi_{D_{(m)}}}} \cdot \left[\frac{j_w + \cancel{\mathcal{B}(e_{\mathcal{K}} - 1)} - j_w \cdot \frac{\chi_{F_{(m)}}}{\chi_{D_{(m)}}} \cdot e_{\mathcal{K}} - \cancel{\mathcal{B}(e_{\mathcal{K}} - 1)} - e_{\Delta T} \cdot \frac{\gamma_i}{\chi_{D_{(m)}}} \cdot \mathcal{B}(e_{\mathcal{K}} - 1)}{j_w + \mathcal{B} \cdot (e_{\mathcal{K}} - 1)}\right]$$

$$= \frac{1}{1 - \frac{\chi_{F_{(m)}}}{\chi_{D_{(m)}}}} \cdot \left[\frac{1 - \frac{\chi_{F_{(m)}}}{\chi_{D_{(m)}}} \cdot e_{\mathcal{K}} - e_{\Delta T} \cdot \frac{\gamma_i}{\chi_{D_{(m)}} \cdot j_w} \cdot \mathcal{B}(e_{\mathcal{K}} - 1)}{1 + \frac{\mathcal{B}}{j_w} \cdot (e_{\mathcal{K}} - 1)}\right]$$

$$= \frac{1}{1 - \frac{\chi_{F_{(m)}}}{\chi_{D_{(m)}}}} \cdot \Lambda \tag{A.43}$$

Consequently, $\Delta\pi_{\text{eff}}$ can be written as,

$$\Delta\pi_{\text{eff}} = \frac{\Delta\pi}{1 - \frac{\chi_{F_{(m)}}}{\chi_{D_{(m)}}}} \cdot \Lambda \tag{A.44}$$

$\Delta\pi$ can be rewritten in terms of concentrations, cf. the Van't hoff law so that,

$$\Delta\pi_{\text{eff}} = \left(\frac{\rho_{mix}}{MW_{mix}} \cdot \beta \cdot R\bar{T}\right) \cdot \frac{\chi_{D_{(m)}} - \chi_{F_{(m)}}}{1 - \frac{\chi_{F_{(m)}}}{\chi_{D_{(m)}}}} \cdot \Lambda = \left(\frac{\rho_{mix}}{MW_{mix}} \cdot \beta \cdot R\bar{T}\right) \cdot \frac{\cancel{\chi_{D_{(m)}} - \chi_{F_{(m)}}}}{\left(\frac{\cancel{\chi_{D_{(m)}} - \chi_{F_{(m)}}}}{\chi_{D_{(m)}}}\right)} \cdot \Lambda$$

$$= \left(\frac{\rho_{mix}}{MW_{mix}} \beta \cdot R\bar{T}\right) \cdot \chi_{D_{(m)}} \cdot \Lambda = \pi_{D_{(m)}} \cdot \Lambda \tag{A.45}$$

Now, consider equation (A.27),

$$j_w = \mathcal{A} \cdot \left(\left[R\bar{T} \left\{ \chi_{w,0} - \gamma_{w,0} \cdot e_{\Delta T} - e^{'}_{\Delta\pi,\Delta T} \cdot e_{\Delta P} \left(\chi_{w,0} - \gamma_{w,0} \cdot e_{\Delta T} \right) \right\} \right] \cdot \frac{1}{\chi_{w,0} \cdot v_w} \right)$$

with the exponential term,

$$e^{'}_{\Delta\pi,\Delta T} = \exp\left(v_w \frac{\Delta\pi_{\text{eff}} + \Delta T \cdot R \cdot v_w^{-1}}{R\bar{T}} \right) = \exp\left(v_w \frac{\overbrace{\pi_{D_{(m)}} \cdot \Lambda}^{\text{(A.45)}} + \Delta T \cdot R \cdot v_w^{-1}}{R\bar{T}} \right)$$

Henceforth, j_w in equation (A.27) is now coupled implicitly, with Λ via the modified exponential, $e^{'}_{\Delta\pi,\Delta T}$.

$$\Lambda = \left[\frac{1 - \frac{\chi_{F_{(m)}}}{\chi_{D_{(m)}}} \cdot e_{\mathcal{K}} - e_{\Delta T} \cdot \frac{\gamma_i}{\chi_{D_{(m)}} \cdot j_w} \cdot \mathcal{B}(e_{\mathcal{K}} - 1)}{1 + \frac{\mathcal{B}}{j_w} \cdot (e_{\mathcal{K}} - 1)} \right] \tag{A.46}$$

Appendix: Ridder's method for root finding

B

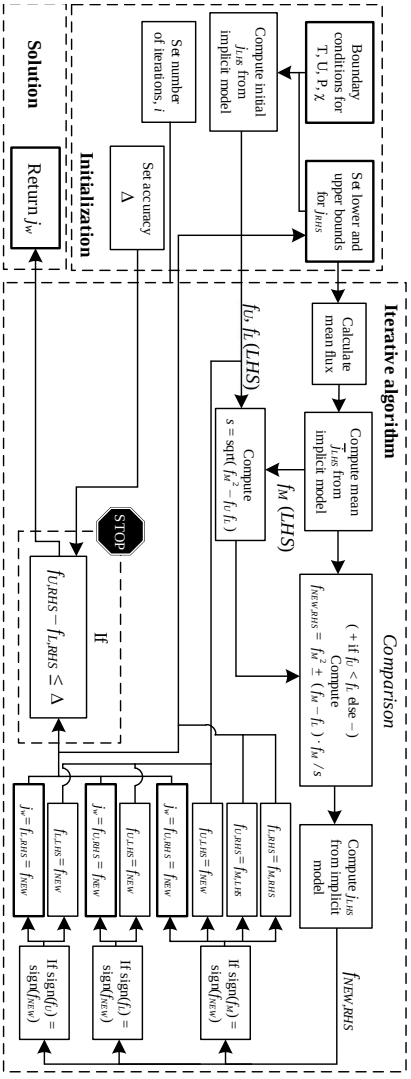

Figure B.1: Overview of the work flow of Ridder's method applied for solving the implicit permeation equation.

Appendix: Proposed thermal transport boundary condition

C

This chapter presents a framework with formulae for describing the heat flux through the membrane. The membrane boundary condition in which it should be applied is not fully developed.

Neglecting transient phenomena in the heat flow through the membrane a steady state heat flux equation can be formulated:

$$\begin{aligned} Q &= \overbrace{h_F\left(\bar{T}_F - T_{F_{(m)}}\right)}^{Q_F} = \overbrace{h_D\left(T_{D_{(m)}} - \bar{T}_D\right)}^{Q_D} \\ &= j_w\rho_w c_p(\bar{T}_F - \bar{T}_D) - \underbrace{h_{sl}(T_{(m)} - T_{F_{(m)}})}_{Q_{sl}} - j_s\rho_s c_p\left(\bar{T}_D - \bar{T}_F\right) - \underbrace{h_{al}(T_{D_{(m)}} - T_{(m)})}_{Q_{al}} \end{aligned} \tag{C.1}$$

This model links the heat transfer in the boundary layers on either side of the membrane with the membrane internal heat transfer. Equation (C.1) can be rearranged into equations (C.2) and (C.3) where $(j_w\rho_w + j_s\rho_s)\cdot\left(\bar{T}_D - \bar{T}_F\right)c_p$ is negligible considering the orders of magnitude: $\mathcal{O}(j_w)\cdot\mathcal{O}(\rho)\cdot\mathcal{O}(\Delta T)\cdot\mathcal{O}(c_p) = 10^{(-7+3+1+0)} = 10^{-3}$ and $\mathcal{O}(h_{al})\cdot\mathcal{O}(T) = 10^{(3+2)} = 10^5$.

$$\begin{aligned} T_{F_{(m)}} &= \frac{h_F\bar{T}_F\left(1+\frac{h_{al}}{h_D}\right) + \cancel{(j_w\rho_w + j_s\rho_s)\cdot\left(\bar{T}_D - \bar{T}_F\right)c_p} + (h_{sl}-h_{al})\,T_{(m)} + h_{al}\bar{T}_D}{h_F\left(1+\frac{h_{al}}{h_D}\right) + h_{sl}} \\ &= \frac{h_F\bar{T}_F\left(1+\frac{h_{al}}{h_D}\right) + (h_{sl}-h_{al})\,T_{(m)} + h_{al}\bar{T}_D}{h_F\left(1+\frac{h_{al}}{h_D}\right) + h_{sl}} \end{aligned} \tag{C.2}$$

$$\begin{aligned} T_{D_{(m)}} &= \frac{h_D\bar{T}_F\left(1+\frac{h_{sl}}{h_F}\right) + \cancel{(j_w\rho_w + j_s\rho_s)\cdot\left(\bar{T}_F - \bar{T}_D\right)c_p} + (h_{al}-h_{sl})\,T_{(m)} + h_{sl}\bar{T}_F}{h_D\left(1+\frac{h_{sl}}{h_F}\right) + h_{al}} \\ &= \frac{h_D\bar{T}_F\left(1+\frac{h_{sl}}{h_F}\right) + (h_{al}-h_{sl})\,T_{(m)} + h_{sl}\bar{T}_F}{h_D\left(1+\frac{h_{sl}}{h_F}\right) + h_{al}} \end{aligned} \tag{C.3}$$

The internal temperature $T_{(m)}$ can be formulated as a weighted function from these two predictions of the temperatures on either side of the membrane:

$$T_{(m)} = \frac{t_a h_{al}\cdot T_{D_{(m)}} + t_s h_{sl}\cdot T_{F_{(m)}}}{t_a h_{al} + t_s h_{sl}} \tag{C.4}$$

These three equations comprise a set of linear equations from which the temperatures in and around the membrane can be calculated assuming that values for the heat transfer coefficients h_D, h_F, h_{sl}, h_{al} are known.

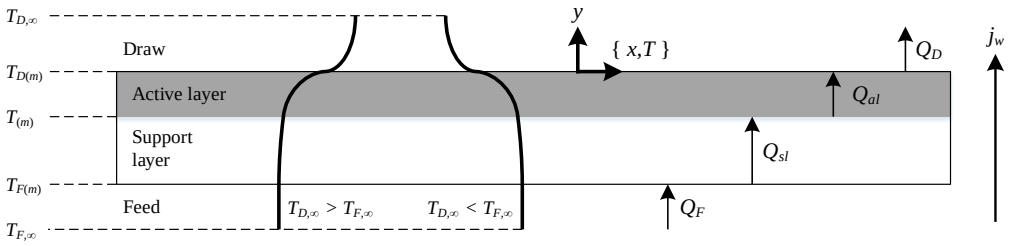

Figure C.1: Nomenclature of local temperatures and schematic of the two possible temperature profiles.

Appendix: Implementation of the membrane boundary

D

There are several ways of setting up an internal boundary with varying difficulty. In many situations, when creating an internal boundary (also commonly termed *baffle*) with a meshing tool such as Pointwise, the least cumbersome approach for creating one is to create the geometry as one block and then separating it into two blocks. The alternative is to create one block in one application, and then creating the internal boundary with another utility, such as the OF utilities `topoSet` and `createBaffles`. This is however more challenging as (i) the spatial discretization of the cells on either side of the internal boundary is difficult to perform and (ii) it is easier to create mismatching cell faces at the interface of the two subsequent blocks. The utilized procedure will now be outlined. A graphic representation is found in Figure D.1.

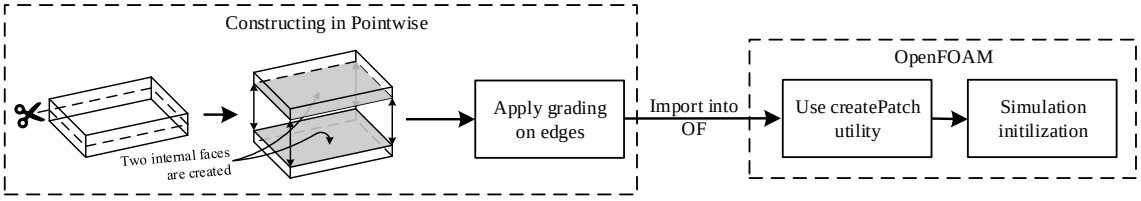

Figure D.1: Simplest method for creating the internal boundary.

This approach makes the creation of the internal boundary relatively effortless and gives little room for error. For the utilized command in OF refer to appendix B on page 79. The following procedure is performed to construct the mesh in Pointwise:

1. Create the vertices of the feed and draw channels, including four vertices that bound the membrane as the internal boundary (12 vertices as in Figure 3.1).
2. Apply grading to the edges, so the boundary layers near the membrane on both sides are sufficiently resolved.
3. Create discretized faces between edges. Two internal faces, incident with the membrane are created, and so are two blocks instead of one.
4. Apply boundary conditions in Pointwise. For the two internal faces, group them under the same group name and boundary condition type *patch*.
5. Export the case file into OF format so that a polyMesh folder is created, with the five files, *boundary, neighbours, faces, owner* and *points*. These files are transferred to the polyMesh folder in the OF case directory. This imports the mesh into OF.

In OF, the membrane boundary is created with the utility `createPatch`.